

Enhanced Meta-Displays Using Advanced Phase-Change Materials

Omid Hemmatyar^{1,†}, Sajjad Abdollahramezani^{1,†}, Ioannis Zeimpekis², Sergey Lepeshov³, Alex Krasnok⁴, Asir Intisar Khan⁵, Kathryn M. Neilson⁵, Christian Teichrib⁶, Tyler Brown¹, Eric Pop⁵, Daniel W. Hewak², Matthias Wuttig⁶, Andrea Alù^{4,7}, Otto L. Muskens⁸, and Ali Adibi¹

¹*School of Electrical and Computer Engineering, Georgia Institute of Technology, 778 Atlantic Drive NW, Atlanta, Georgia 30332-0250, US*

²*Zepler Institute, Faculty of Engineering and Physical Sciences, University of Southampton, SO17 1BJ Southampton, United Kingdom*

³*ITMO University, St. Petersburg 197101, Russia*

⁴*Photonics Initiative, Advanced Science Research Center, City University of New York, New York, New York 10031, United States*

⁵*Department of Electrical Engineering, Department of Materials Science and Engineering, Precourt Institute for Energy, Stanford University, Stanford, California 94305, United States*

⁶*Physikalisches Institut IA, RWTH Aachen, Sommerfeldstrasse 14, 52074 Aachen, Germany*

⁷*Physics Program, Graduate Center, City University of New York, New York, New York 10016, United States*

⁸*Physics and Astronomy, Faculty of Engineering and Physical Sciences, University of Southampton, SO17 1BJ Southampton, United Kingdom, and*

[†]*These authors contributed equally to this work.*

(Dated: July 27, 2021)

Structural colors generated due to light scattering from static all-dielectric metasurfaces have successfully enabled high-resolution, high-saturation, and wide-gamut color printing applications. Despite recent advances, most demonstrations of these structure-dependent colors lack post-fabrication tunability. This hinders their applicability for front-end dynamic display technologies. Phase-change materials (PCMs), with significant contrast of their optical properties between their amorphous and crystalline states, have demonstrated promising potentials in reconfigurable nanophotonics. Herein, we leverage tunable all-dielectric reflective metasurfaces made of newly emerged classes of low-loss optical PCMs, i.e., antimony trisulphide (Sb_2S_3) and antimony triselenide (Sb_2Se_3), with superb characteristics to realize switchable, high-saturation, high-efficiency and high-resolution dynamic meta-pixels. Exploiting polarization-sensitive building blocks, the presented meta-pixel can generate two different colors when illuminated by either one of two orthogonally polarized incident beams. Such degrees of freedom (i.e., material phase and polarization state) enable a single reconfigurable metasurface with fixed geometrical parameters to generate four distinct wide-gamut colors. We experimentally demonstrate, for the first time, an electrically-driven micro-scale display through the integration of phase-change metasurfaces with an on-chip heater formed by transparent conductive oxide. Our experimental findings enable a versatile platform suitable for a wide range of applications, including tunable full-color printing, enhanced dynamic displays, information encryption, and anti-counterfeiting.

INTRODUCTION

In the past decades, absorption and emission of light from organic dyes and chemical pigments have been the most common color generation mechanisms in color-imaging and display devices [1]. Nevertheless, there are still several challenges with the developed technologies, such as environmental hazards, vulnerability to high-intensity light, and limited scalability to smaller pixel sizes. In order to address these issues, structural colors have emerged as compelling alternatives. Structural colors are observed in numerous natural species, whose bright features arise from light scattering and interference in micro/nanostructured patterns of their skins or scales [2]. Inspired by nature and enabled by recent advancement in nanofabrication, artificial structural colors generated via a resonant interaction between incident white light and miniaturized building blocks in optical metasurfaces [3–6], i.e., arrays of subwavelength patterned nanostructures, have gained great attention in recent years. In

this context, plasmonic metasurfaces made of gold, silver and aluminum nanostructures have been extensively used to generate structural colors based on plasmon resonances [7]. Despite their versatility, the broad and weak plasmon resonances, imposed by the significant inherent ohmic loss of the constituent metallic materials, result in low color saturation and purity [8].

To meet the challenges associated with plasmonic metasurfaces, recently, all-dielectric metasurfaces made of high-refractive-index materials supporting Mie-type resonances with electric dipole (ED) and magnetic dipole (MD) modes have been used for generating a full range of vivid and highly saturated structural colors desired for high-resolution display technologies [9–12]. However, these colors are fixed-by-design and cannot be tuned since the geometrical parameters of passive all-dielectric metasurfaces cannot be changed after fabrication. In order to enable active display applications, a real-time color tunability is essential.

To realize high-resolution structural color tunability in metasurfaces, several modulation techniques have been

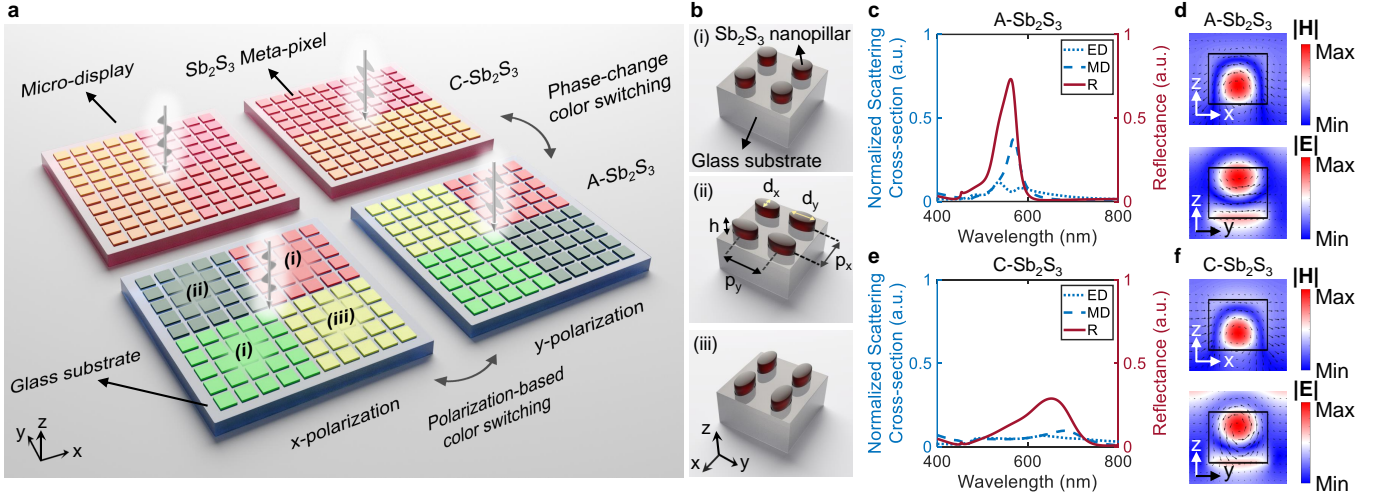


Figure 1. **Working principle of a polarization-encoded dynamic display composed of phase-change meta-pixels.** **a,b**, Schematic representation of a reflective display consisting of phase-change meta-pixels. Each meta-pixel is a metasurface formed by a periodic arrangement of Sb_2S_3 nanopillars shown in **(b)**, which can generate four different colors; two colors for each polarization attributed to the amorphous and crystalline phases of Sb_2S_3 (i.e. A- Sb_2S_3 and C- Sb_2S_3 , respectively) nanopillars or two colors for each Sb_2S_3 phase (corresponding to x-polarized and y-polarized incident white light). For all metasurfaces, the height (h) of the nanopillars is fixed while their periodicity in x- and y-directions (i.e., p_x and p_y , respectively) change to generate different colors. The major and minor axes of the nanopillars in x- and y-directions are proportional to the corresponding periodicities in those directions with a constant aspect ratio, i.e. $d_{x,y} = \alpha p_{x,y}$, in which α is constant. The colors shown in **(a)** correspond to Sb_2S_3 metasurfaces with (i) $p_x = p_y = 310$ nm (for green) and $p_x = p_y = 390$ nm (for red), (ii) $p_x = 310$ nm, $p_y = 390$ nm, and (iii) $p_x = 390$ nm and $p_y = 310$ nm, with $\alpha = 0.6$ and $h = 120$ nm. **c-f**, Multipolar decomposition analysis: **c,e**, Calculated normalized scattering cross-sections and simulated reflectance (R) spectrum of a Sb_2S_3 metasurface with geometrical parameters of $p_{x,y} = 310$ nm, $d_{x,y} = 0.6 p_{x,y}$, and $h = 120$ nm for the **(c)** amorphous and **(e)** crystalline phases. The constructive interference between the electric dipole (ED) and magnetic dipole (MD) modes at $\lambda_a = 560$ nm ($\lambda_c = 652$ nm) boosts the backward scattering intensity, and in turn, results in a reflectance peak in the case of A- Sb_2S_3 (C- Sb_2S_3). **d,f**, Normalized magnetic field intensity with arrow surface of electric field (top panel), and normalized electric field intensity with arrow surface of magnetic field (bottom panel) for the metasurfaces in **(b)** at **(d)** $\lambda_a = 560$ nm and **(f)** $\lambda_c = 652$ nm, respectively.

proposed. Some examples are liquid crystals in conjunction with plasmonic nanoantennae [13, 14], utilizing mechanically stretchable substrates integrated with plasmonic [15] and dielectric [16] nanoscatterers, changing the refractive index of the medium surrounded nanostructures [17], modifying the optical properties of the constituent magnesium-based nano-cavities of a hybrid plasmonic-dielectric platform via a chemical reaction [18], and changing the polarization state of incident light [19]. Despite impressive advancements, these approaches can hardly meet the requirements for lightweight, flexible, durable, high-resolution, high-speed, and cost-effective dynamic color displays with high color contrast and saturation, multiple stable colors, and high refreshing rates.

To overcome the existing shortcomings, chalcogenide phase-change materials (PCMs) [20–34], with optical properties (e.g., refractive index) that can be strongly modified upon applying an external stimulus (optical, electrical, or thermal), have been successfully used as tunable materials for color switching [35–39]. The advantages of PCM-based color-switching techniques over other counterparts originate from unique electrical and optical features of PCMs including nonvolatility, high in-

dex contrast, fast reversible switching speeds (10s-100s nanoseconds) between two stable phases, high durability (up to 10^{12} cycles), notable scalability (down to nm-scale sizes), good thermal stability (up to several hundred degrees), and adaptability with the CMOS fabrication technology [22]. Considering these unique features, single [35, 36] or multiple ultrathin films [37] made of germanium antimony telluride (GST in short) and germanium telluride (GeTe) alloys in a multistack configuration with other dielectric and/or metallic films have been utilized for color switching [38]. In spite of the unparalleled properties of PCMs, these demonstrations suffer from the high absorption loss of GST and GeTe within the visible wavelength range, which results in low-quality-factor (low-Q) reflectance resonances. This, in turn, yields colors with low saturation, low color value (i.e., the reflectance value at the resonance peak) and purity in both amorphous and crystalline states of these PCMs.

To address these challenges, here we systematically design and experimentally demonstrate an actively tunable platform for color displays comprising all-dielectric metasurfaces formed by a geometrical arrangement of phase-change nanoellipsoids. We leverage a less explored class

of PCMs, i.e., antimony trisulphide (Sb_2S_3) and antimony triselenide (Sb_2Se_3), exhibiting low-loss property in the visible spectral range [40–45]. Due to their high refractive indices, these materials support strong Mie-type ED and MD resonances. The sensitivity of these modes on refractive index enables high-resolution (up to $\sim 80,000$ dots per inch (dpi)) phase-transition-based color switching with high saturation and purity [11]. Moreover, owing to the polarization-sensitivity of the constituent asymmetric PCM nanopillars, we can encode two different colors into two mutually orthogonal polarization states of the incident light. This results in realization of a display with fixed geometrical parameters that can generate four different colors upon transition in the structural state of the contributed PCM. Finally, the integration of an electrically controlled transparent heater with the polarization-encoded phase-change meta-pixels, reported for the first time in this work, enables real-time reconfiguration for applications ranging from tunable full-color printing and displays, information encryption, and anti-counterfeiting to wearable screens and electronic papers.

RESULTS AND DISCUSSION

Figure 1a demonstrates the operation principle of a dynamic display formed by phase-change meta-pixels. Each meta-pixel is composed of a periodic array of rectangular unit cells, with different periodicity along x- and y-directions (i.e., p_x and p_y in Fig. 1b (ii)), containing asymmetric elliptical Sb_2S_3 nanopillars on top of a glass substrate. The major and minor axes of the Sb_2S_3 nanopillars are proportional to the periodicity of the unit cell in the corresponding directions, i.e., $d_{x,y} = \alpha p_{x,y}$, in which α is fixed between 0 and 1. The height of the nanopillars (h) is constant for the fabrication preference. The reflected color upon normally incident x-polarized white light can change by varying the geometrical parameters of the elliptical amorphous- Sb_2S_3 (A- Sb_2S_3) nanopillars or equivalently those of the unit cell (see the bottom-left display in Fig. 1a). Upon phase transition, crystalline- Sb_2S_3 (C- Sb_2S_3) nanopillars with the same geometrical parameters and under the same illumination conditions generate colors that are different from those generated by their A- Sb_2S_3 counterparts (compare the top and bottom displays in Fig. 1a). This phase-change color switching is attributed to the refractive index change of the constituent Sb_2S_3 meta-pixels upon transition between amorphous and crystalline phases.

To reveal the switching mechanism of, we performed the multipole decomposition analysis of the scattering spectrum of a Sb_2S_3 meta-pixel under white light illumination, as shown in Figs. 1c-f (see Supporting Information Note I and Fig. S1 for more details). The analysis shows negligible contribution of the higher-order moments so that the optical response of the unit cell is governed by the electric dipole (ED) and magnetic dipole (MD) moments. In fact, the strong coupling between

these refractive index-dependent ED and MD moments excited inside the Sb_2S_3 nanopillars with the directly reflected light yields the resonances in the reflectance spectra shown in Figs. 1c,e. Therefore, the spectral position of these resonances, or equivalently the generated color by a meta-pixel under a specific polarized light, is determined by the refractive index of the Sb_2S_3 nanopillars. In addition to the color switching mechanism described above, the asymmetric nature of nanopillars can enable a polarization-based color switching in which one meta-pixel can generate different colors upon white light illumination with different polarization states (i.e., x- to y-polarization) in each phase of Sb_2S_3 (compare the left and right displays in Fig. 1a). Therefore, one meta-pixel with fixed geometrical parameters can generate four different colors owing to the phase-change-tunability and polarization-sensitivity of the constituent Sb_2S_3 nanopillars.

To study the effect of material phase on the generated color, we first consider polarization-insensitive meta-pixels with a square lattice ($p_x = p_y = p$) and circular ($d_x = d_y = d$) Sb_2S_3 nanopillars. We set the geometrical parameters as $h = 120$ nm and $d = 0.65p$ while we vary the periodicity of the unit cell from $p = 290$ nm to $p = 450$ nm, with a step of 20 nm, to cover a wide range of possible colors. The corresponding reflectance spectra obtained from full-wave simulations (see Method), and in turn, the generated colors are shown in Fig. 4a. The method used for obtaining the associated colors with each reflectance spectrum is detailed in Supporting Information Note II and Fig. S3. As shown in Fig. 4a, by increasing p , the spectral position of the resonance peaks for both amorphous (solid lines) and crystalline (dashed lines) states red-shift. Moreover, switching the phase of the material shifts the resonance peak to the longer wavelengths. This is due to positive refractive index contrast ($\Delta n_{\text{Sb}_2\text{S}_3} = n_{\text{C-Sb}_2\text{S}_3} - n_{\text{A-Sb}_2\text{S}_3} > 0$) within the visible wavelength range (see Supplementary Fig. S2c). The higher absorption loss of C- Sb_2S_3 mean that the nanopillars in the crystalline state (dashed lines in Fig. 2a) do not support equally strong and sharp resonances as seen for A- Sb_2S_3 (solid lines).

To demonstrate the validity of our approach, we fabricated and characterized $50 \times 50 \mu\text{m}^2$ Sb_2S_3 meta-pixels with the same design parameters as those in Fig. 4a (see Methods for fabrication and characterization details). The measured reflectance spectra, associated colors observed under the microscope as well as magnified top-view scanning electron micrographs (SEMs) of fabricated meta-pixels are shown in Fig. 4b demonstrating an overall good agreement with the results obtained from simulations. To qualitatively analyze the performance of the presented color generation/switching mechanism in terms of saturation maintenance and hue variation, we display the generated colors in the amorphous (black circles) and crystalline (white squares) phases in the same International Commission on Illumination (CIE) 1931 chromaticity coordinates in Fig. 4c. While for green-

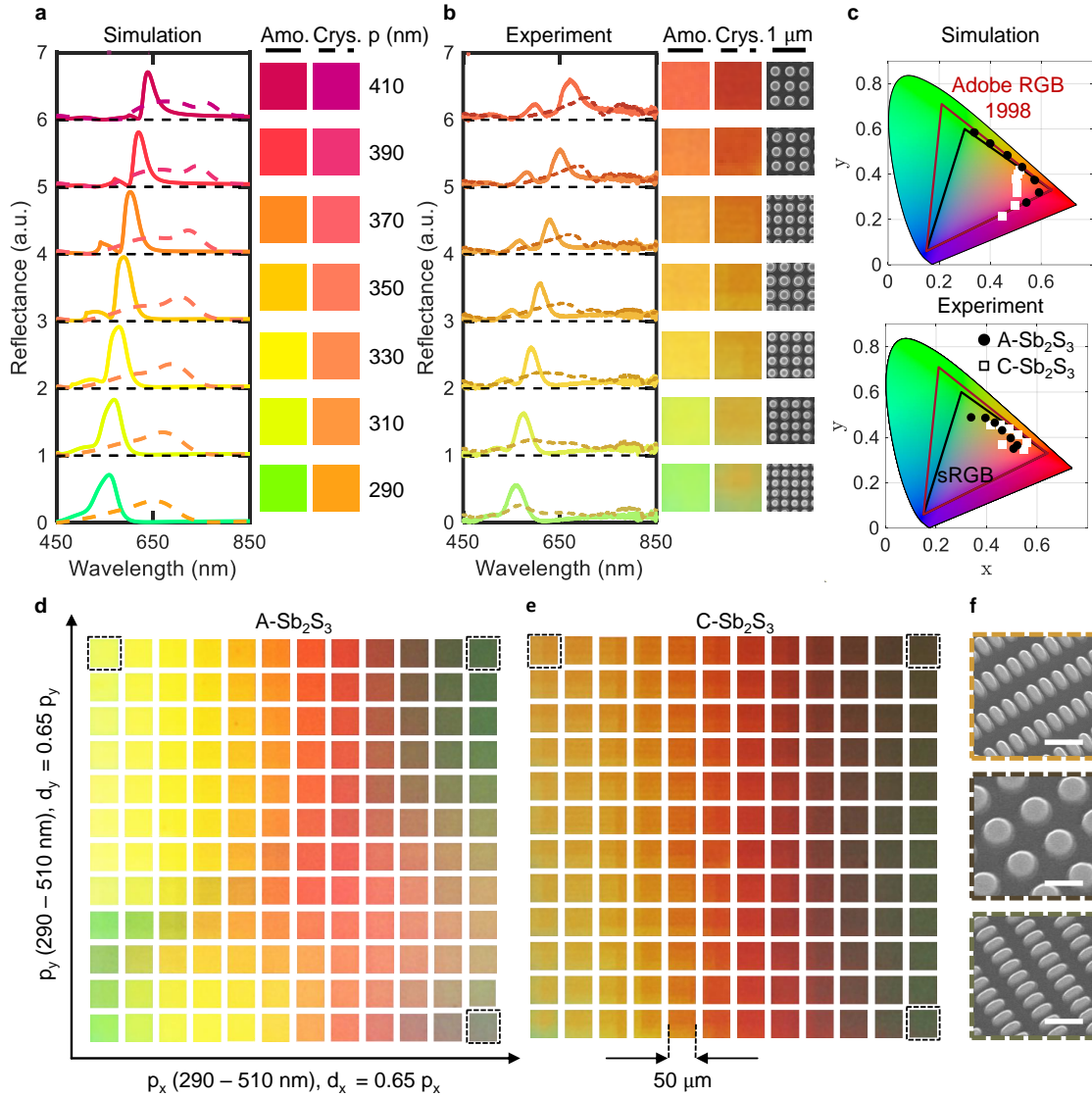


Figure 2. Simulation results and experimental characterization of polarization-encoded dynamic phase-change meta-pixels. **a,b**, Simulated (**a**) and experimental (**b**) reflectance spectra for the polarization-insensitive A-Sb₂S₃ (solid lines) and C-Sb₂S₃ (dashed lines) metasurfaces as well as their corresponding colors and SEM images for different periodicity ($p_x = p_y = p$). The curves are displaced vertically for better visibility and comparison. The diameter of Sb₂S₃ nanopillars varies as $d = 0.65p$. The sharp resonances observed in (**a**) and (**b**) are attributed to the interference between ED and MD modes inside the Sb₂S₃ nanopillars as shown in Figs. 1(c)-(f) causing the spectral position of these resonances become refractive-index-dependent. Therefore, red-shifting is observed upon phase transition of Sb₂S₃. **c**, Corresponding CIE 1931 chromaticity coordinates of the reflectance spectra shown in (**a,b**) for A-Sb₂S₃ (black circles) and C-Sb₂S₃ (white squares). **d,e**, The color palettes for the fabricated (**d**) A-Sb₂S₃ and (**e**) C-Sb₂S₃ meta-pixels considering different periodicity in x- and y-directions (p_x and p_y , respectively) varying with 20 nm increments. **f**, SEM images showing magnified bird's eye views of three meta-pixels indicated by dashed boxes in (**d,e**). The scale bar in (**f**) is 500 nm. The height of the Sb₂S₃ nanopillars is fixed at $h = 120$ nm. The images of color pixels are captured through a $2.5\times$ objective lens with numerical aperture (NA) of 0.075.

ish and reddish colors, both simulation and experimental results demonstrate high saturation values (i.e., those markers close to the edge of the gamut), the purplish colors cannot be produced in the experiments. We attribute this to the presence of undesired secondary peaks observed in the reflectance spectra in Fig. 4b for $p > 390$ nm due to fabrication imperfections. A thorough quanti-

tative study on the color gamut coverage, saturation, and hue for the case of Sb₂S₃ meta-pixels and an other low-loss PCM (i.e., Sb₂Se₃) is presented in Supplementary Note III and Figs. S4,5.

In order to add polarization sensitivity to our color-switching approach, from now on, we also consider elliptical nanopillars in asymmetric unit cells with differ-

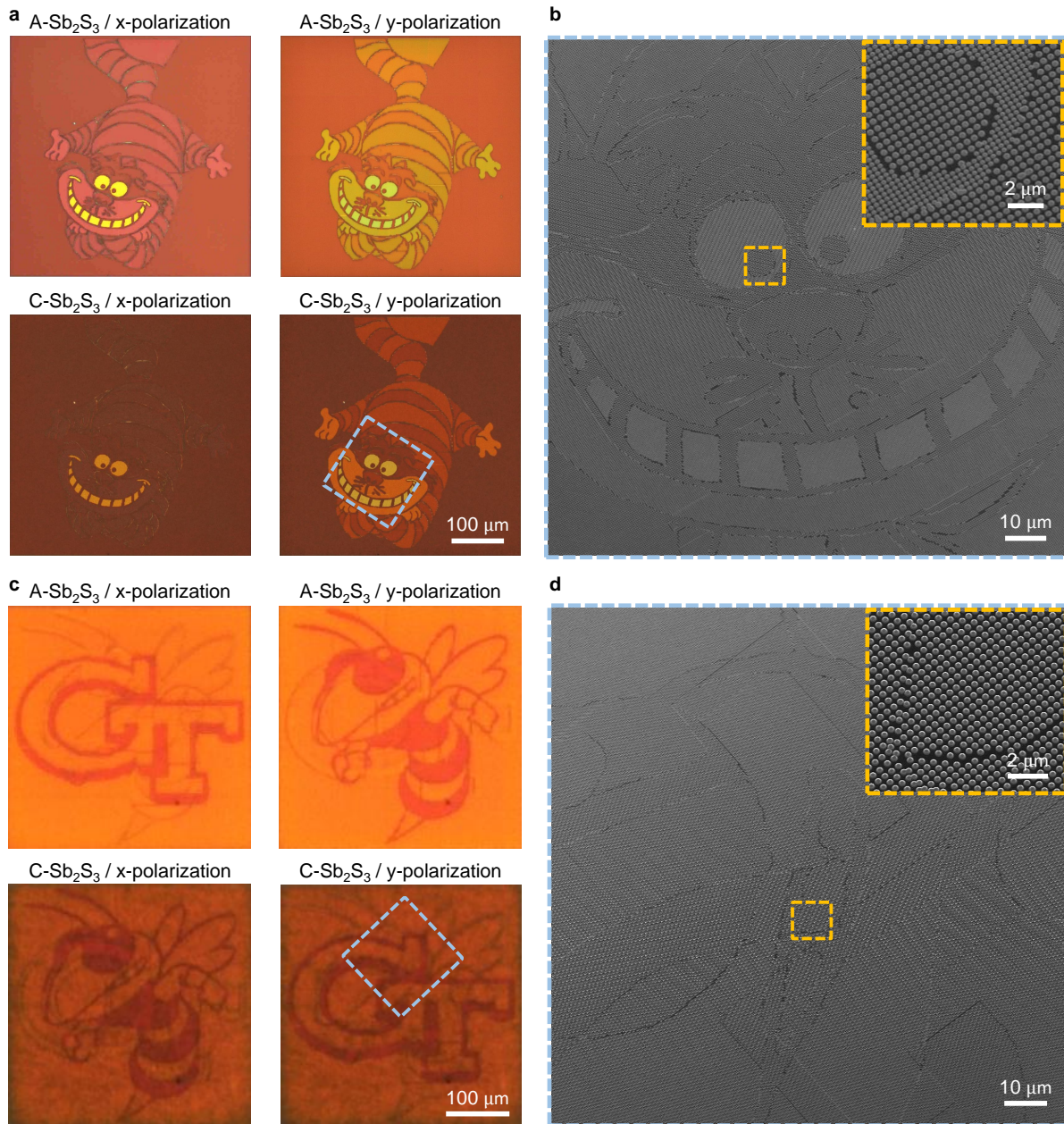


Figure 3. Dynamic displays enabled by polarization-sensitive Sb_2S_3 meta-pixels. **a**, Reproduction of the image of The Cheshire Cat by A- Sb_2S_3 and C- Sb_2S_3 meta-pixels. For the case of A- Sb_2S_3 , switching the polarization of incident white light changes the generated color throughout the image. This phenomenon is also observed for incident y -polarized light upon crystallization of A- Sb_2S_3 . Under x -polarization, however, all parts of The Cheshire Cat body in the amorphous phase vanish except its teeth and eyes upon switching to the crystalline phase. This is also the case when changing the polarization of the incident white light from y - to the x -direction in the crystalline phase. **b**, The SEM image of the fabricated array of Sb_2S_3 nanopillars associated with the face of The Cheshire Cat indicated by the blue dashed box shown in (a). The magnified SEM image shown in the inset demonstrates that a meta-pixel containing only four Sb_2S_3 nanopillars is capable of generating the desired color justifying the high-resolution nature of the presented color-printing approach. **c**, Encryption of two images (i.e., Georgia Tech logo and symbol) into a display containing an engineered arrangement of Sb_2S_3 meta-pixels. One image can be switched to another either by changing the polarization of incident light in each phase, or by changing the phase of the Sb_2S_3 meta-pixels under the same polarization. The latter is the first experimental demonstration of encryption of two totally different images into the phase of the constituent material of meta-pixels. **d**, The SEM image of the fabricated Sb_2S_3 meta-pixels corresponding to the blue dashed box shown in (c). The design strategy and geometrical parameters of different parts of the images shown in (a-d) is explained in Supplementary Figs. S15-17. The images in (a) and (c) are captured through $10\times$ ($\text{NA} = 0.3$) and $2.5\times$ ($\text{NA} = 0.075$) objective lenses, respectively.

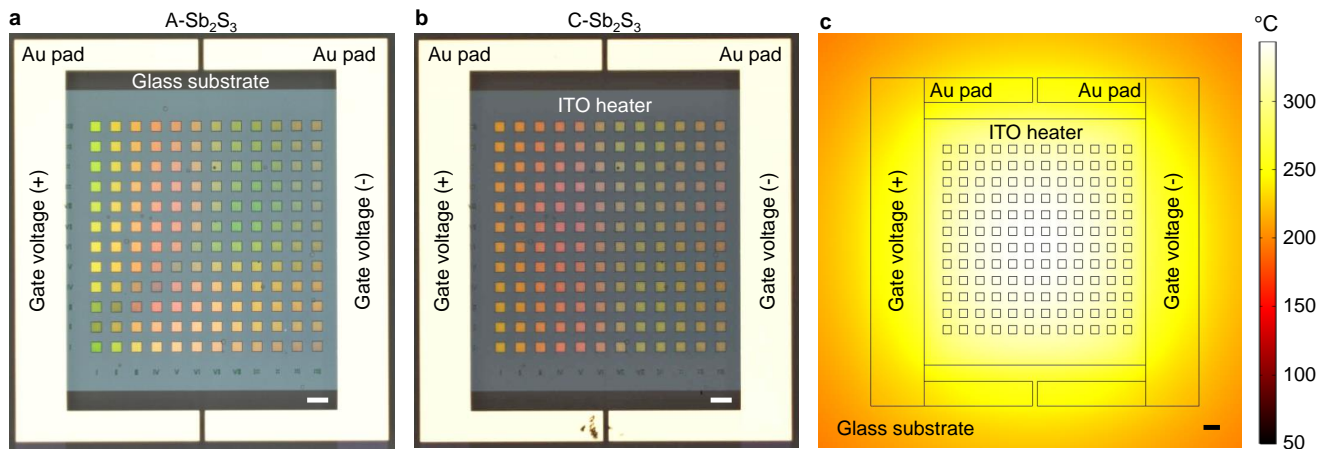


Figure 4. **Electrically driven dynamic color display device integrating a transparent heater.** **a,b,** The bright-field microscope images of the electrically tunable color palettes comprising $50 \times 50 \mu\text{m}^2$ (a) A-Sb₂S₃ and (b) C-Sb₂S₃ meta-pixels fabricated on a glass substrate and encapsulated by a 150 nm-thick film of SiO₂. The transparent heater is formed by fabrication of a 50 nm-thick ITO bridge connecting Au probing pads at the two ends on top of the SiO₂ film. The geometrical parameters of the Sb₂S₃ meta-pixels shown in (a) and (b) are similar to those used in Fig. 4 (d,e). The images are captured using a $2.5\times$ objective (NA = 0.075). **c,** Simulated stationary temperature map in the cross section of Sb₂S₃ meta-pixels in the course of applying a 27 V electrical signal to the Au probing pads. The uniform heat distribution across the palettes ensures realization of large-scale displays with selective controllability of the material phase of all meta-pixels. The scale bars are 100 μm .

ent periodicity in the x- and y-directions, i.e., p_x and p_y , as shown in Fig. 1b. By varying p_x and p_y from 290 nm to 510 nm with a 20-nm increment and a fixed ratio with respect to the major and minor axes of the nanopillars (i.e., $d_{x,y} = 0.65 p_{x,y}$), we fabricate the color palettes shown in Figs. 4d,e captured under x-polarized illumination. Measurement under y-polarization yields the same pattern flipped in p_x and p_y (results not shown here). The magnified bird's eye view of three meta-pixels indicated by dashed boxes in Fig. 4d,e are displayed in Fig. 4f. The simulated palettes as well as a detailed analysis on the polarization-based and phase-change-based color switching approaches in the presented platform considering both Sb₂S₃ and Sb₂Se₃ meta-pixels are provided in Supplementary Note IV and Figs. S6-9. In addition to the ratio used in Fig. 4d,e (i.e., $\alpha = 0.65$), we fabricate palettes of meta-pixels with other ratios of 0.45 and 0.55 and plot the captured images in Supplementary Fig. S10. Moreover, based on the simulation results in Supplementary Fig. S8, we design and fabricate palettes of Sb₂Se₃ meta-pixels with different ratios and display their microscopic images in Fig. S11. The sensitivity of the generated colors to the polarization angle, incident angle, and different design parameters of the meta-pixels are analyzed in Supplementary Notes V (Fig. S12), VI (Fig. S13), and VII (Fig. S14), respectively.

The color switching enabled by the phase transition of Sb₂S₃ and polarization of the incident light can be employed for implementation of a dynamic display. According to the color palettes in Figs. 4d,e, under x- (y-) polarization, a column (row) of different colors in the amorphous phase can be mapped onto a column (row) of relatively similar colors in the crystalline phase. We

leverage this unique feature of the Sb₂S₃ meta-pixels for switching off some parts of an image while maintaining the colors of the remaining parts. As an illustrative example, the image of The Cheshire Cat is generated by A-Sb₂S₃ meta-pixels illuminated with x-polarized white light as shown in Fig. 3a (i). Upon phase-transition to the C-Sb₂S₃, all parts of the body vanish, but the grinning and eyes remain (see Fig. 3a (ii)). It is also the case when changing the polarization state from y to x in the crystalline phase. On the other hand, altering the polarization in amorphous phase as well as switching the material phase under y-polarization result only in a variation of colors in the components of the image. The SEM image of the fabricated array of Sb₂S₃ nanopillars associated with the face of The Cheshire Cat indicated by the blue dashed box shown in Fig. 3a is displayed in Fig. 3b. The magnified SEM image shown in the inset demonstrates that a meta-pixel containing only four Sb₂S₃ nanopillars can generate the desired color showing the high-resolution nature of the presented approach. The geometrical parameters of the meta-pixels used for the generation of Figs. 3a,b are tabulated in Supplementary Fig. S15.

Another interesting characteristic of our platform is its two degrees of freedom, i.e., phase-change and polarization-based color switching, at the same time. In fact, it is possible to darken (brighten) some parts of an image using the polarization-based control, while brightening (darkening) other parts using phase-change control of the meta-pixels. We benefit from this capability to encrypt two different images (i.e., Georgia Tech logo and symbol) into a display containing an array of Sb₂S₃ meta-pixels as shown in Fig. 3c. One image can be switched

to another one either by altering the polarization in each material phase, or by changing the phase of the Sb_2S_3 meta-pixels under a fixed polarization. While the former has been reported in previous works, the latter, to the best of our knowledge, is the first demonstration of encryption of two totally different images into the phase of the constituent materials of a meta-pixel. The SEM image of the fabricated Sb_2S_3 meta-pixels corresponding to the blue dashed box in Fig. 3c is demonstrated in Fig. 3d. The design strategy of the meta-pixels used for generating Figs. 3c,d is provided in Supplementary Fig. S16. Moreover, we demonstrate other examples of dynamic displays using Sb_2Se_3 meta-pixels in Supplementary Fig. S17. For the case of Sb_2Se_3 , we demonstrate the encoding and decoding of four different images into the A- Sb_2Se_3 (ON-state) and C- Sb_2Se_3 (OFF-state), respectively, under x- and y-polarizations. These capabilities can be used in many applications such as information coding, cryptography, high-density optical data storage, security encryption, and 3D displays.

In all experiments shown in Figs. 1-3, the phase-transition in our Sb_2S_3 meta-pixels is performed by using a bulky heater for a relatively long annealing time (see Methods for details). Though laser pulses can be used to expedite the conversion process [45], the on-chip integration of high-power fast lasers is challenging if not impossible. This hinders the applicability of our approach for on-demand compact, high-resolution, fast, and on-chip display. To promote the presented approach to a practical paradigm, we must electrically convert the Sb_2S_3 meta-pixels. Recently, electrical switching of PCMs based on Joule heating has been successfully demonstrated using metal micro-heaters [27, 33, 34]. However, none of these platforms is suitable for structural color generation due to the excessive loss of their constituent material in the visible range. Thanks to their reduced optical loss, micro-heater formed in transparent conductive oxides hold the promise to enable next-generation dynamic structural colors.

As a proof-of-concept demonstration, we leverage an indium tin oxide (ITO) heater to electrically reconfigure the phase-change meta-pixels without compromising the quality of the generated colors. To this end, the fabricated palettes in Figs. 4d,e are first encapsulated by a SiO_2 layer followed by fabrication of a 50 nm-thick indium tin oxide (ITO) bridge connecting two gold (Au) probing pads at the two ends on top of the SiO_2 film (see Figs. 4a,b and Methods for fabrication details). The electro-thermal simulation in Fig. 4c illustrates that a fairly uniform heat distribution can be realized across the whole area of the display upon applying the voltage pulse ensuring simultaneous and uniform conversion of all palettes. Such a Joule heating platform offers the precise electrical control of the intermediate phases of PCMs (beyond amorphous and crystalline) which is critical for realization of multicolor displays, a key attribute of our approach. We further investigate the potential of ITO-based micro-heater for reversible switching of colors

in Supplementary Information Figs. S19-22.

CONCLUSION

In summary, we demonstrated here a new platform for generating and switching high-efficiency, high-saturation, and wide-gamut structural colors using switchable meta-pixels by employing PCM-based metasurfaces made of low-loss and less explored Sb_2S_3 and Sb_2Se_3 nanopillars. Upon the nonvolatile phase-transition of the constituent PCM, the generated color in the amorphous phase switches to a distinctive stable color in the crystalline phase. In addition, the properly designed asymmetric characteristics of elliptical nanopillars enable polarization-based color switching. Combining these two tuning mechanisms, we systematically designed a single-layer meta-pixel capable of producing four different colors. This can be extended to the realization of multi-color artificial images by gradually changing the crystallinity of the constituent PCMs and/or the incident polarization angle. We also showed that by engineering the arrangement of PCM-based nanopillars, features like image switching, ON/OFF switching, and color shading can be realized. More interestingly, we experimentally demonstrate, for the first time, an electrically driven micro-scale display by integration of an optically-transparent heater to our color without compromising the color quality. We believe that this research provides a significant step towards the realization and commercialization of compact metaphotonic devices for applications like full-color dynamic displays, information storage, image encryption, and anti-counterfeiting.

ACKNOWLEDGEMENTS

The work was primarily funded by the Office of Naval Research (ONR) (N00014-18-1-2055, Dr. B. Bennett) and by the Air Force Office of Scientific Research MURI program. The support of the UK's Engineering and Physical Science Research Centre is gratefully acknowledged, through ChAMP-Chalcogenide Advanced Manufacturing Partnership (EP/M015130/1). The Stanford authors acknowledge partial support from the Stanford Graduate Fellowship, from the Nonvolatile Memory Technology Research Initiative (NMTRI), and from Draper Labs. This work was performed in part at the Georgia Tech Institute for Electronics and Nanotechnology (IEN), a member of the National Nanotechnology Coordinated Infrastructure (NNCI), which is supported by NSF (ECCS1542174).

DISCLOSURES

The authors declare no conflicts of interest.

METHODS

Sample fabrication. The fabrication flow for the Sb_2S_3 metasurface and integrated transparent heater of the meta-display is illustrated in Fig. S23. A Sb_2S_3 film of nominally 130 nm thickness is first sputtered on a cleaned fused silica substrate from a stoichiometric target followed by the deposition of a 15-nm thick $\text{ZnS}:\text{SiO}_2$ film serving as a protective layer to prevent oxidation and elemental loss of Sb_2S_3 undergoing the heating process. Next, the sample is coated with a layer of hydrogen silsesquioxane (HSQ) negative e-beam resist and a thin water-soluble conductive layer of ESpacer to hamper the charge accumulation during the writing process. E-beam lithography is then performed to define the nanopillar pattern in each $50 \times 50 \mu\text{m}^2$ meta-pixel. After washing out ESpacer using DI water, the exposed photoresist is developed by subsequently immersing it in a bath of 25% tetramethylammonium hydroxide (TMAH) and rinsing with gently flowing DI water. Inductively couple plasma reactive ion etching (ICP-RIE) is performed with a gas mixture of Ar: CF_4 with the etching rate of ~ 75 nm/min to form nanostructure patterns. The etching process is conducted through two 1-min cycles with a long-enough cooldown break in between. Right after the etching, a 15 nm protective layer of SiO_2 is grown on the sample using atomic layer deposition (ALD) at 100°C , which is low enough to prevent the crystallization of Sb_2S_3 . To convert the material state of Sb_2S_3 to the crystalline phase, the sample is annealed at 270°C for 10 mins in a chamber filled with an ultrahigh pure Ar gas.

To realize the electrically-driven display, the fabricated sample (excluded from the annealing process) is first transferred to the ALD system to deposit a 200-nm thick layer of thermal SiO_2 as a supporting substrate for the integrated heater. After defining the pattern of the ITO bridge in the polymethyl methacrylate (PMMA)-coated sample using e-beam lithography, a 50 nm-thick layer of ITO is deposited by the RF-magnetron sputtering from an indium oxide/tin oxide ($\text{In}_2\text{O}_3/\text{SnO}_2$ with 90/10 wt %) target in an argon/oxygen plasma atmosphere. The prolonged nature of the deposition facilitates the crystallization of ITO necessary for the formation of a uniform conductive layer enabling spatially consistent heat generation. After the lift-off process, to further enhance the electrical conductivity of the ITO film, post-deposition annealing under a mild flow of oxygen, which also reduces the optical loss of ITO, is conducted at 200°C for 30 mins. This temperature is low enough to preclude crystallization of as-deposited Sb_2S_3 . Two Au/Ti (250/20 nm) electrodes are formed at the two ends of the ITO bridge through subsequent e-beam lithography and e-beam evaporation processes. After the lift-off process, in the final step, a 100 nm layer of SiO_2 is grown to prevent the failure of the heater caused by the electric breakdown of the air at the sharp corners of the device. To fully transform the Sb_2S_3 phase from amorphous to crystalline based on the Joule heating process, a 32 V long-enough

(1 min) pulse is applied to the integrated heater using a source measurement unit (Keithley 2614B).

Optical measurements. To investigate the optical response of the fabricated meta-displays, bright-field optical imaging and reflection spectra measurements of the color palettes are conducted. Optical images are captured using a conventional upright bright-field reflection microscope (Nikon ECLIPSE L200, Nikon Inc.) equipped with a high-definition color camera head (DS-Fi2) and a 50 W halogen lamp light source. To observe different colors of The Cheshire Cat and Georgia Tech logo and symbol images under different polarization states of incident white light, the corresponding images are magnified with a $10\times$ objective lens ($\text{NA} = 0.3$) and a $2.5\times$ objective lens ($\text{NA} = 0.075$), respectively, under illumination of polarized light in both orthogonal directions. The optical spectra ($\lambda = 450\text{-}850$ nm) are measured in reflection mode using a home-built microscope set-up equipped with a 75 W broadband xenon source (Newport) and a UV-visible-near infrared (NIR) spectrometer (USB 2000+, Ocean Optics Inc.). The polarized light illuminates a colour palette at normal incidence through an achromatic $10\times$ objective lens ($\text{NA} = 0.25$) and is collected through the same objective and back into the spectrometer and a CCD camera. The measured reflectance spectra are normalized to the reflected light from an aluminium-coated mirror. All measurements are carried out at room temperature ($\sim 25^\circ\text{C}$).

Numerical simulations. The full-wave simulations of the reflectance spectra of the metasurfaces are performed using the commercial software Lumerical Solutions based on the finite-different time-domain (FDTD) technique. The periodic boundary condition is used in the x- and y-directions to mimic the periodicity, while perfectly matched layers are used in the z-direction (top and bottom layers) to model the free space. The refractive index of the glass substrate is set at 1.46 for the entire wavelength range. The dispersive optical constants of PCMs obtained from spectroscopic ellipsometry measurements shown in Supplementary Fig. S2 are incorporated into simulations.

Electro-thermal simulations. A three-dimensional finite element method (FEM) simulation is performed in the software package COMSOL Multiphysics to simulate the Joule heating and heat dissipation effects in the electrified hybrid display. In our simulations, we consider certain assumptions and boundary conditions to mimic the experimental conditions. The multiphysics problem is solved through coupling of an electric currents (ec) module to a heat transfer in solid (ht) physics model. Material properties used for fused silica, Ti, Au, and ITO are adopted from the available references [46, 47]. The electrical conductivity of ITO obtained from the four-point probe measurement is set at 1.42×10^4 S/m. The thermal conductivity, density, and heat capacity of Sb_2S_3 are 1.16 W/m·K, 4600 kg/m³, and 120 J/mol·K, respectively [45]. The ec module is applied to the ITO bridge and electrodes. Electric insulation are assigned to all boundaries

except for the two endfaces of the bridge where normal current density and electric ground are applied. The ht physics model is assigned to all domains. The convective cooling boundary condition with an ambient temperature

of 20 °C and the heat transfer coefficient of 5 W/m².K is used at the top and bottom surfaces. Open boundary condition is applied to the walls of the substrate in the lateral directions.

-
- [1] S. Daqiqeh Rezaei, Z. Dong, J. You En Chan, J. Trisno, R. J. H. Ng, Q. Ruan, C.-W. Qiu, N. A. Mortensen, and J. K. Yang, Nanophotonic structural colors, *ACS Photonics* (2020).
- [2] P. Vukusic, J. Sambles, C. Lawrence, and R. Wootton, Quantified interference and diffraction in single morpho butterfly scales, *Proceedings of the Royal Society of London. Series B: Biological Sciences* **266**, 1403 (1999).
- [3] N. Yu, P. Genevet, M. A. Kats, F. Aieta, J.-P. Tetienne, F. Capasso, and Z. Gaburro, Light propagation with phase discontinuities: generalized laws of reflection and refraction, *Science* **334**, 333 (2011).
- [4] A. E. Krasnok, A. E. Miroschnichenko, P. A. Belov, and Y. S. Kivshar, All-dielectric optical nanoantennas, *Optics Express* **20**, 20599 (2012).
- [5] M. Decker, I. Staude, M. Falkner, J. Dominguez, D. N. Neshev, I. Brener, T. Pertsch, and Y. S. Kivshar, High-efficiency dielectric huygens' surfaces, *Advanced Optical Materials* **3**, 813 (2015).
- [6] A. I. Kuznetsov, A. E. Miroschnichenko, M. L. Brongersma, Y. S. Kivshar, and B. Luk'yanchuk, Optically resonant dielectric nanostructures, *Science* **354** (2016).
- [7] X. Duan, S. Kamin, and N. Liu, Dynamic plasmonic colour display, *Nature Communications* **8**, 1 (2017).
- [8] A. Kristensen, J. K. Yang, S. I. Bozhevolnyi, S. Link, P. Nordlander, N. J. Halas, and N. A. Mortensen, Plasmonic colour generation, *Nature Reviews Materials* **2**, 1 (2016).
- [9] X. Zhu, W. Yan, U. Levy, N. A. Mortensen, and A. Kristensen, Resonant laser printing of structural colors on high-index dielectric metasurfaces, *Science Advances* **3**, e1602487 (2017).
- [10] B. Yang, W. Liu, Z. Li, H. Cheng, D.-Y. Choi, S. Chen, and J. Tian, Ultrahighly saturated structural colors enhanced by multipolar-modulated metasurfaces, *Nano Letters* **19**, 4221 (2019).
- [11] O. Hemmatyar, S. Abdollahramezani, Y. Kiarashinejad, M. Zandehshahvar, and A. Adibi, Full color generation with fano-type resonant hfo 2 nanopillars designed by a deep-learning approach, *Nanoscale* **11**, 21266 (2019).
- [12] W. Yang, S. Xiao, Q. Song, Y. Liu, Y. Wu, S. Wang, J. Yu, J. Han, and D.-P. Tsai, All-dielectric metasurface for high-performance structural color, *Nature Communications* **11**, 1 (2020).
- [13] D. Franklin, Y. Chen, A. Vazquez-Guardado, S. Modak, J. Boroumand, D. Xu, S.-T. Wu, and D. Chanda, Polarization-independent actively tunable colour generation on imprinted plasmonic surfaces, *Nature Communications* **6**, 1 (2015).
- [14] J. Olson, A. Manjavacas, T. Basu, D. Huang, A. E. Schlather, B. Zheng, N. J. Halas, P. Nordlander, and S. Link, High chromaticity aluminum plasmonic pixels for active liquid crystal displays, *ACS Nano* **10**, 1108 (2016).
- [15] M. L. Tseng, J. Yang, M. Semmlinger, C. Zhang, P. Nordlander, and N. J. Halas, Two-dimensional active tuning of an aluminum plasmonic array for full-spectrum response, *Nano Letters* **17**, 6034 (2017).
- [16] P. Gutruf, C. Zou, W. Withayachumnankul, M. Bhaskaran, S. Sriram, and C. Fumeaux, Mechanically tunable dielectric resonator metasurfaces at visible frequencies, *ACS Nano* **10**, 133 (2016).
- [17] N. S. King, L. Liu, X. Yang, B. Cerjan, H. O. Everitt, P. Nordlander, and N. J. Halas, Fano resonant aluminum nanoclusters for plasmonic colorimetric sensing, *ACS Nano* **9**, 10628 (2015).
- [18] Y. Chen, X. Duan, M. Matuschek, Y. Zhou, F. Neubrech, H. Duan, and N. Liu, Dynamic color displays using stepwise cavity resonators, *Nano Letters* **17**, 5555 (2017).
- [19] B. Yang, W. Liu, Z. Li, H. Cheng, S. Chen, and J. Tian, Polarization-sensitive structural colors with hue-and-saturation tuning based on all-dielectric nanopixels, *Advanced Optical Materials* **6**, 1701009 (2018).
- [20] M. Wuttig, H. Bhaskaran, and T. Taubner, Phase-change materials for non-volatile photonic applications, *Nature Photonics* **11**, 465 (2017).
- [21] F. Ding, Y. Yang, and S. I. Bozhevolnyi, Dynamic metasurfaces using phase-change chalcogenides, *Advanced Optical Materials* **7**, 1801709 (2019).
- [22] S. Abdollahramezani, O. Hemmatyar, H. Taghinejad, A. Krasnok, Y. Kiarashinejad, M. Zandehshahvar, A. Alù, and A. Adibi, Tunable nanophotonics enabled by chalcogenide phase-change materials, *Nanophotonics* **9**, 1189 (2020).
- [23] B. Gholipour, J. Zhang, K. F. MacDonald, D. W. Hewak, and N. I. Zheludev, An all-optical, non-volatile, bidirectional, phase-change meta-switch, *Advanced Materials* **25**, 3050 (2013).
- [24] Y. Zhang, J. B. Chou, J. Li, H. Li, Q. Du, A. Yadav, S. Zhou, M. Y. Shalaginov, Z. Fang, H. Zhong, *et al.*, Broadband transparent optical phase change materials for high-performance nonvolatile photonics, *Nature Communications* **10**, 1 (2019).
- [25] H. Taghinejad, S. Abdollahramezani, A. A. Eftekhar, T. Fan, A. H. Hosseinnia, O. Hemmatyar, A. E. Dorche, A. Gallmon, and A. Adibi, Ito-based microheaters for reversible multi-stage switching of phase-change materials: towards miniaturized beyond-binary reconfigurable integrated photonics, *Optics Express* **29**, 20449 (2021).
- [26] C. Ríos, M. Stegmaier, P. Hosseini, D. Wang, T. Scherer, C. D. Wright, H. Bhaskaran, and W. H. Pernice, Integrated all-photonic non-volatile multi-level memory, *Nature Photonics* **9**, 725 (2015).
- [27] S. Abdollahramezani, O. Hemmatyar, M. Taghinejad, H. Taghinejad, A. Krasnok, A. A. Eftekhar, C. Teichrib, S. Deshmukh, M. El-Sayed, E. Pop, *et al.*, Electrically driven programmable phase-change meta-switch reaching 80% efficiency, *arXiv preprint arXiv:2104.10381* (2021).
- [28] J. Tian, H. Luo, Y. Yang, F. Ding, Y. Qu, D. Zhao,

- M. Qiu, and S. I. Bozhevolnyi, Active control of anapole states by structuring the phase-change alloy $\text{Ge}_{2}\text{Sb}_{2}\text{Te}_{5}$, *Nature Communications* **10**, 1 (2019).
- [29] A.-K. U. Michel, A. Heßler, S. Meyer, J. Pries, Y. Yu, T. Kalix, M. Lewin, J. Hanss, A. De Rose, T. W. Maß, *et al.*, Advanced optical programming of individual meta-atoms beyond the effective medium approach, *Advanced Materials* **31**, 1901033 (2019).
- [30] S. Abdollahramezani, O. Hemmatyar, M. Taghinejad, H. Taghinejad, Y. Kiarashinejad, M. Zandehshahvar, T. Fan, S. Deshmukh, A. A. Eftekhari, W. Cai, *et al.*, Dynamic hybrid metasurfaces, *Nano Letters* **21**, 1238 (2021).
- [31] C. Wu, H. Yu, S. Lee, R. Peng, I. Takeuchi, and M. Li, Programmable phase-change metasurfaces on waveguides for multimode photonic convolutional neural network, *Nature Communications* **12**, 1 (2021).
- [32] J. Zheng, Z. Fang, C. Wu, S. Zhu, P. Xu, J. K. Doylend, S. Deshmukh, E. Pop, S. Dunham, M. Li, *et al.*, Non-volatile electrically reconfigurable integrated photonic switch enabled by a silicon pin diode heater, *Advanced Materials* **32**, 2001218 (2020).
- [33] Y. Zhang, C. Fowler, J. Liang, B. Azhar, M. Y. Shalaginov, S. Deckoff-Jones, S. An, J. B. Chou, C. M. Roberts, V. Liberman, *et al.*, Electrically reconfigurable non-volatile metasurface using low-loss optical phase-change material, *Nature Nanotechnology* **16**, 661 (2021).
- [34] Y. Wang, P. Landreman, D. Schoen, K. Okabe, A. Marshall, U. Celano, H.-S. P. Wong, J. Park, and M. L. Brongersma, Electrical tuning of phase-change antennas and metasurfaces, *Nature Nanotechnology* **16**, 667 (2021).
- [35] P. Hosseini, C. D. Wright, and H. Bhaskaran, An optoelectronic framework enabled by low-dimensional phase-change films, *Nature* **511**, 206 (2014).
- [36] S. Tao, Q. Li, J. Wang, X. Wang, J. Cai, S. Li, W. Xu, K. Zhang, and C. Hu, Phase change materials for non-volatile, solid-state reflective displays: From new structural design rules to enhanced color-changing performance, *Advanced Optical Materials* **8**, 2000062 (2020).
- [37] S. Yoo, T. Gwon, T. Eom, S. Kim, and C. S. Hwang, Multicolor changeable optical coating by adopting multiple layers of ultrathin phase change material film, *ACS Photonics* **3**, 1265 (2016).
- [38] S. G.-C. Carrillo, L. Trimby, Y.-Y. Au, V. K. Nagareddy, G. Rodriguez-Hernandez, P. Hosseini, C. Ríos, H. Bhaskaran, and C. D. Wright, A nonvolatile phase-change metamaterial color display, *Advanced Optical Materials* **7**, 1801782 (2019).
- [39] C. R. de Galarreta, I. Sinev, A. M. Alexeev, P. Trofimov, K. Ladutenko, S. G.-C. Carrillo, E. Gemo, A. Baldycheva, J. Bertolotti, and C. D. Wright, Reconfigurable multilevel control of hybrid all-dielectric phase-change metasurfaces, *Optica* **7**, 476 (2020).
- [40] C. Ghosh and B. Varma, Optical properties of amorphous and crystalline $\text{Sb}_{2}\text{S}_{3}$ thin films, *Thin solid films* **60**, 61 (1979).
- [41] C. Chen, W. Li, Y. Zhou, C. Chen, M. Luo, X. Liu, K. Zeng, B. Yang, C. Zhang, J. Han, *et al.*, Optical properties of amorphous and polycrystalline $\text{Sb}_{2}\text{Se}_{3}$ thin films prepared by thermal evaporation, *Applied Physics Letters* **107**, 043905 (2015).
- [42] W. Dong, H. Liu, J. K. Behera, L. Lu, R. J. Ng, K. V. Sreekanth, X. Zhou, J. K. Yang, and R. E. Simpson, Wide bandgap phase change material tuned visible photonics, *Advanced Functional Materials* **29**, 1806181 (2019).
- [43] M. Delaney, I. Zeimpekis, D. Lawson, D. W. Hewak, and O. L. Muskens, A new family of ultralow loss reversible phase-change materials for photonic integrated circuits: $\text{Sb}_{2}\text{S}_{3}$ and $\text{Sb}_{2}\text{Se}_{3}$, *Advanced Functional Materials*, 2002447 (2020).
- [44] M. Delaney, I. Zeimpekis, H. Du, X. Yan, M. Banakar, D. J. Thomson, D. W. Hewak, and O. L. Muskens, Nonvolatile programmable silicon photonics using an ultralow-loss $\text{Sb}_{2}\text{Se}_{3}$ phase change material, *Science Advances* **7**, eabg3500 (2021).
- [45] H. Liu, W. Dong, H. Wang, L. Lu, Q. Ruan, Y. S. Tan, R. E. Simpson, and J. K. Yang, Rewritable color nanoprints in antimony trisulfide films, *Science Advances* **6**, eabb7171 (2020).
- [46] D. R. Lide, *CRC handbook of chemistry and physics*, Vol. 85 (CRC press, 2004).
- [47] C. Rios, M. Stegmaier, Z. Cheng, N. Youngblood, C. D. Wright, W. H. Pernice, and H. Bhaskaran, Controlled switching of phase-change materials by evanescent-field coupling in integrated photonics, *Optical Materials Express* **8**, 2455 (2018).
- [48] J. D. Jackson, *Classical electrodynamics* (1999).
- [49] P. Grahm, A. Shevchenko, and M. Kaivola, Electromagnetic multipole theory for optical nanomaterials, *New Journal of Physics* **14**, 093033 (2012).
- [50] S. D. Rezaei, R. J. Hong Ng, Z. Dong, J. Ho, E. H. Koay, S. Ramakrishna, and J. K. Yang, Wide-gamut plasmonic color palettes with constant subwavelength resolution, *ACS nano* **13**, 3580 (2019).

SUPPLEMENTARY INFORMATION

I. MULTIPOLAR DECOMPOSITION

Electromagnetic properties of the nanoparticles in the arrays are numerically studied by using the commercial software CST Microwave StudioTM. In the canonical basis we perform a multipole expansion of the scattered field of the hybrid nanoparticles into vector spherical harmonics, which form a complete and orthogonal basis allowing the unique expansion of any vectorial field. To calculate electric ($a_E(l,m)$) and magnetic ($a_M(l,m)$) spherical multipole coefficients, we project the scattered electric field \mathbf{E}_{sca} on a spherical surface, enclosing the nanoparticles centered at the symmetric point of the nanodisc, onto vector spherical harmonics based on the following relations [48, 49]:

$$a_E(l, m) = \frac{(-i)^{l+1} k R}{h_l^{(1)}(kR) E_0 \sqrt{\pi(2l+1)(l+1)l}} \int_0^{2\pi} \int_0^\pi Y_{lm}^*(\theta, \phi) \mathbf{r} \mathbf{E}_{sca}(\mathbf{r}) \sin \theta d\theta d\phi, \quad (\text{S.1})$$

$$a_M(l, m) = \frac{(-i)^l k R}{h_l^{(1)}(kR) E_0 \sqrt{\pi(2l+1)}} \int_0^{2\pi} \int_0^\pi \mathbf{X}_{lm}^*(\theta, \phi) \mathbf{E}_{sca}(\mathbf{r}) \sin \theta d\theta d\phi, \quad (\text{S.2})$$

where R is the radius of the enclosing sphere, k is the wavenumber, $h_l^{(1)}$ is the Hankel function with the asymptotic of the outgoing spherical wave, E_0 is the amplitude of the incident wave, Y_{lm}^* and \mathbf{X}_{lm}^* are scalar and vector spherical harmonics. The integers l and m describe the order of the multipole (dipole, quadrupole, ...) and the amount of the z -component of angular momentum that is carried per photon, respectively. Due to the azimuthal symmetry of the nanoparticles under normal excitation, the amplitude of the scattering coefficients with opposite m indices are identical, i.e., $a_{E,M}(l, m) = a_{E,M}(l, -m)$.

II. COLOR GENERATION

To achieve generated colors, the International Commission on Illumination (CIE) XYZ tristimulus values corresponding to the reflection spectra are calculated as [11]:

$$\begin{aligned} X &= \frac{1}{k} \int I(\lambda) R(\lambda) \bar{x}(\lambda) d\lambda, \\ Y &= \frac{1}{k} \int I(\lambda) R(\lambda) \bar{y}(\lambda) d\lambda, \\ Z &= \frac{1}{k} \int I(\lambda) R(\lambda) \bar{z}(\lambda) d\lambda \end{aligned} \quad (\text{S.3})$$

where k is the normalization factor, $I(\lambda)$ is energy distribution of the reference light; $R(\lambda)$ is the reflection spectrum obtained from the designed metasurface under illumination; and $\bar{x}(\lambda)$, $\bar{y}(\lambda)$, and $\bar{z}(\lambda)$ are the CIE 1931 standard color-matching functions (see Figure S2a). These chromaticity functions are then normalized as $x = X/(X+Y+Z)$ and $y = Y/(X+Y+Z)$, which fall between 0 to 1, to represent the colors in the CIE 1931 chromaticity diagram.

III. QUANTITATIVE ANALYSIS ON COLOR GAMUT COVERAGE, SATURATION MAINTENANCE AND HUE VARIATION

As shown in Fig. S4d-f, by increasing p , the spectral position of the reflectance resonances for both amorphous (solid lines) and crystalline (dashed lines) states red-shifts. The spectral position of each of these resonances is dependent on the refractive index of the constituent phase-change material (PCM) owing to the interference between ED and MD modes inside the PCM nanopillars as will be discussed later. Therefore, by switching the state of the nanopillars from amorphous to crystalline, the central wavelengths of the resonances red-shift in the cases of Sb_2S_3 and Sb_2Se_3 (see Fig. S4d,e), and blue-shift in the case of GeSe_3 (see Fig. S4f) because $\Delta n_{\text{Sb}_2\text{S}_3}$, $\Delta n_{\text{Sb}_2\text{Se}_3} > 0$, while $\Delta n_{\text{GeSe}_3} < 0$ (with $\Delta n = n_{\text{C-PCM}} - n_{\text{A-PCM}}$) within the visible wavelength range (see the refractive indices in Fig. S2a,b). The actual shift of the resonance wavelengths are $|\Delta \lambda_{\text{Sb}_2\text{S}_3}| < 180$ nm, $|\Delta \lambda_{\text{Sb}_2\text{Se}_3}| < 200$ nm, and $|\Delta \lambda_{\text{GeSe}_3}| < 70$ nm (see Fig. S4d-f). The relative strength of the wavelength shifts in these PCMs, i.e. $|\Delta \lambda_{\text{Sb}_2\text{Se}_3}| > |\Delta \lambda_{\text{Sb}_2\text{S}_3}| > |\Delta \lambda_{\text{GeSe}_3}|$, is attributed to the relative strength of the change in the real part of their refractive indices upon the phase transition between amorphous and crystalline, i.e. $|\Delta n_{\text{Sb}_2\text{Se}_3}| > |\Delta n_{\text{Sb}_2\text{S}_3}| > |\Delta n_{\text{GeSe}_3}|$, as shown in Supplementary Fig. S1. On the other hand, the sharpness of the reflectance resonances in Fig S4d-f is mainly dependent on the PCM extinction coefficient shown as the dashed curves in Fig. S4e,f. In the case of Sb_2S_3 nanopillars, the high-efficiency resonances (i.e., those with high reflectance value at the resonance peak) in the low-loss amorphous phase are damped upon the transition to the crystalline phase with higher absorption loss (compare solid and dashed curves in Fig. S4d). This high absorption loss arises for both amorphous and crystalline Sb_2Se_3 nanopillars, resulting in relatively low-efficiency reflectance resonances (see Fig. S4f). In contrast, GeSe_3 nanopillars remain very low-loss across the entire visible range for both the amorphous and crystalline phases, yielding high-efficiency resonances in both cases (see Fig. S4f).

For a quantitative comparison between the presented three PCMs in terms of color generation/switching, Figs. 4g-i show the generated colors in the amorphous (black circles) and crystalline (white squares) phases

in the same International Commission on Illumination (CIE) 1931 chromaticity coordinates for the three PCMs in top panels, and their corresponding hue and saturation values for amorphous (solid-circle lines) and crystalline (dashed-square curves) phases in the bottom panels. The approach of calculating the CIE XYZ tristimulus of the reflectance spectra and their corresponding hue and saturation values are given in the Supporting Information Note I. In terms of the color gamut coverage, the calculated color gamut area for A-Sb₂Se₃ (C-Sb₂Se₃) is around 98.3% (43.4%) of the standard RGB (sRGB) and 72.9% (32.2%) of the Adobe RGB, from Fig. 4g. The color gamut area for the case of A-Sb₂Se₃ (C-Sb₂Se₃) is around 70.1% (33.3%) of the sRGB, and 52% (24.7%) of the Adobe RGB (from Figure 4h). For the case of A-GeSe₃ (C-GeSe₃), a full-range of colors with gamut area of 57.8% (90.8%) of the sRGB, and 42.9% (67.3%) of the Adobe RGB can be obtained (from Figure 4i). Therefore, in terms of color gamut area, Sb₂S₃ and GeSe₃ have almost the same performance, yet better than Sb₂Se₃. Moreover, these results show that our all-dielectric PCM-based metasurfaces can generate a wide color gamut larger than the state-of-the-art plasmonic colors ($\sim 45\%$ of sRGB [50]) for A-Sb₂S₃, A-Sb₂Se₃ and A/C-GeSe₃ cases.

In the RGB color-mixing model, the hue (H) is defined as the proportion of the dominant wavelength (resonance wavelength in this case) with respect to other wavelengths in the reflected light and is independent of the intensity of the light. It simply indicates the "perceived color" by the human eyes and ranges from 0° to 360°, in which 0° (and 360°), 120° and 240° represent pure red, pure green, and pure blue, respectively (See Supplementary Fig. S3 for more details). The saturation, on the other hand, is defined as the ratio of the intensity of the reflected light at the resonance wavelength (associated to the perceived color) to that of the incident white light, simply indicating the purity of a color and ranging from 0% to 100%. Considering this definition, the narrower the bandwidth of the reflectance resonance, the higher the saturation of the generated color. In the content of color switching between two phases, the performance measure is achieving two highly-saturated colors in both phases with a maximum hue variation ($\Delta H = H_{C-PCM} - H_{A-PCM}$) upon switching. To analyze the performance of the presented phase-transition-based color-switching approach, the hue and saturation values of the simulated colors in Fig. S4d-f are plotted in the bottom panels in Fig. S4g-i for both amorphous (solid-circle lines) and crystalline (dashed-square curves) phases of the PCMs. In terms of saturation preservation upon phase transition, GeSe₃ shows high-saturation values for both amorphous and crystalline cases (due to sharp reflectance resonances), while Sb₂S₃ shows highly saturated colors only in the amorphous phase. Sb₂Se₃, however, demonstrates a median level of saturation values in both amorphous and crystalline phases due to the wide reflectance resonances. With regards to hue varia-

tion, the hues of the generated colors in Sb₂S₃ and GeSe₃ cases change by varying p in both amorphous and crystalline states while maintaining $\Delta H < 80^\circ$ upon phase transition. One may use this feature to switch the coloration of pixels of an image individually with each pixel being a Sb₂S₃ or GeSe₃ metasurface formed by of an array of down to 5×5 or 6×6 nanopillars [11]. In the case of Sb₂Se₃, however, by changing p , all the varying hue values in the amorphous phase switch to an almost fixed hue in the crystalline phase. Using this property, one can turn off all the pixels of an image on a display comprising Sb₂Se₃ metasurfaces (i.e., pixels) by switching the phase of the Sb₂Se₃ nanopillars from the amorphous state (ON-state) to the crystalline state (OFF-state). This is a unique feature that is absent in other approaches in previous works, e.g., the polarization-sensitive color-switching approach [19].

To provide a comparison between Sb₂S₃, Sb₂Se₃, and GeSe₃ metasurfaces for color switching applications, a spider chart is shown in Fig. S5. The figure of merit (FOM) is defined as the maximum variation of the hue over the refractive index change open phase transition between amorphous and crystalline, i.e. $|\Delta \text{Hue}|/|\Delta n|$ in which $\Delta n = n_A(\lambda_A) - n_C(\lambda_C)$, with $n_A(\lambda_A)$ and $n_C(\lambda_C)$ being the index of refraction in the amorphous and crystalline phases and at the corresponding resonance wavelengths (λ_A, λ_C), respectively. While high FOM is desirable, the saturation and value (i.e. the reflectance value at the resonance peak) of the colors in both amorphous and crystalline phases should be as high as possible. Considering all these performance measures, GeSe₃ demonstrates superior properties over Sb₂S₃ and Sb₂Se₃ when switching from a color associated with a reflectance spectrum with a resonance peak at $\lambda = 600$ nm (chosen as the middle wavelength in the visible range from 400 nm to 800 nm) in the amorphous phase, to another color in the crystalline phase.

IV. POLARIZATION-SENSITIVE DYNAMIC COLOR GENERATION

To add the polarization-sensitivity to our color-switching approach, we also consider elliptical nanopillars in asymmetric unit cells with different periodicities in the x- and y-directions, i.e. p_x and p_y , Fig 1b. By varying p_x and p_y with a fixed ratio with respect to the major and minor axes of the nanopillars (i.e., $d_{x,y} = \alpha p_{x,y}$), we generate the color palettes shown in Fig. S6a,d,g, for the case of Sb₂S₃ ($p_{x,y}$ range from 310 nm to 470 nm with 40-nm increments), Sb₂Se₃ ($p_{x,y}$ range from 200 nm to 400 nm with 50-nm increments), and GeSe₃ ($p_{x,y}$ range from 270 nm to 430 nm with 40-nm increments), respectively (see Supplementary Fig. S4-S6 in the for full color palettes). In each figure, the top (bottom) panels show the colors generated by the x-polarized (y-polarized) incident white light for amorphous (left panels) and crystalline (right panels) cases.

While Sb_2S_3 and GeSe_3 metasurfaces can generate a full palette considering both amorphous and crystalline phases (see Fig. S6a,g), respectively, Sb_2Se_3 metasurfaces cannot generate bluish colors (see Fig. S6d). This stems from the high optical loss of Sb_2Se_3 within the blue range of the visible wavelengths (see Fig. S2a,b). It is also clear that the y -polarization palettes can be obtained by transposing the x -polarization palette, i.e., replacing each (j,i) element with corresponding (i,j) element. However, this is not the case for amorphous and crystalline palettes in Fig. S6a,d,g since the crystalline palettes contain completely different colors from those in the amorphous palettes. This shows the advantage of using PCMs as the number of colors in the phase-transition-based color-switching approach is twice as many as those in the polarization-based approach.

To analyze the effect of polarization-sensitivity in both amorphous and crystalline cases on the reflected colors, we select five metasurfaces for each PCM with geometrical parameters in the dashed boxes in Fig. S6a,d,g, and plot the corresponding simulated reflectance spectra with their hue and saturation values in the inset in Fig. S6b,e,h, respectively. It is seen that by increasing p_y in each box, the central wavelength of the reflectance resonances does not experience a considerable shift for the x -polarization (see the top panels in Fig. S6b,e,h). This leads to almost unchanged hue values for the corresponding colors, which in turn results in a limited trajectory in the corresponding color gamuts shown in the top panels of Fig. S6c,f,i in which black circles (white squares) represent the colors in amorphous (crystalline) phase. In contrast, it is observed that increasing p_y results in a tangible redshift in the reflectance spectra for the y -polarization for all PCMs (see the bottom panels in Fig. S6b,e,h). This redshift results in a relatively large hue change in all cases, except C- Sb_2Se_3 , as the corresponding color gamuts in the bottom panels of Fig. S6c,f,i demonstrate. The simulated full color palettes as well as their corresponding gamuts are provided in Figs. S7-9. Based on these simulation results, we designed and fabricated palettes of Sb_2S_3 and Sb_2Se_3 meta-pixels with different ratios and display their corresponding microscopic images in Fig. S12 and 13, respectively.

Finally, in the Supplementary Note V, we show that by continuously varying the incident polarization angle (φ) one can enable dynamic color tuning (See Figure S12).

V. SENSITIVITY TO THE INCIDENT POLARIZATION ANGLE

To analyze the effect of the variation of the incident polarization angle (φ) on the reflected colors, we select one metasurface for each type of PCMs with geometrical parameters shown in Fig. S12a,d,g and change φ from 0° (y -polarization) to 90° (x -polarization). The reflectance spectra of these metasurfaces for $\varphi = 0^\circ$ and $\varphi = 90^\circ$ for both amorphous and crystalline states are plotted in

Fig. S12c,f,i. In both amorphous and crystalline states, a resonance shift of at least 100 nm is observed, which enables us to dynamically tune the reflected colors by varying the incident polarization angle. This polarization-based color tunability is demonstrated in the colors in Fig. S12b,e,h, which are generated through varying φ from 0° to 90° in a step of 15° . The colors in Fig. S12b,e,h and their corresponding CIE diagrams show that using Sb_2S_3 and GeSe_3 metasurfaces, one can tune the colors from green to reddish purple to blue, while Sb_2Se_3 can enable color tuning from dark green to red to purple.

VI. SENSITIVITY TO THE INCIDENT ANGLE

To analyze the effect of the incident angle (θ) on the reflectance spectrum of a metasurface (Fig. 1b), we select a metasurface with Sb_2S_3 nanopillars, as shown in Fig. S13a,b, and vary the angle of the incident light from $\theta = 0^\circ$ to $\theta = 30^\circ$. Fig. S13c,d show the reflection spectra for amorphous Sb_2S_3 , and Fig. S13e,f show the results of crystalline Sb_2S_3 , with TE- and TM-polarized light, respectively. In the case of TE-polarized light incident on amorphous Sb_2S_3 (Fig. S13c), the incident angle has a small impact on the reflection spectrum. The intensity of the reflected is reduced by 20% when θ approaches 5° , but the reflection spectra does not suffer any redshift. The spectra resulted from the crystalline Sb_2S_3 experiences a redshift of more than 100 nm and is less intense and is less intense compared to the amorphous case, but these spectra remain largely unaffected by the incident angle variation.

In the case of TM-polarized light on amorphous Sb_2S_3 , a much greater dependence on θ is observed from Fig. S13d,f. As θ increases, two effects can be seen from these figures: 1) the initial peak at $\theta = 0^\circ$ seen begins to lose intensity and experiences a redshift, and 2) a new peak forms and becomes more pronounced, both as θ goes beyond 5° . When Sb_2S_3 is crystalline in this case, no considerable changes are observed for $0^\circ < \theta < 20^\circ$ after which the peak redshifts by about 100 nm at $\theta = 30^\circ$. In addition, for $\theta > 20^\circ$, the second peak that was observable in the amorphous case is not seen in the crystalline case. These results are not surprising; the reflectance of these metasurfaces is largely due to ED and MD resonances that are supported by the nanopillar structures, and the ED resonances are the dominating resonances seen in the reflectance spectra. Since the component of the electric field parallel to the top surface of the Sb_2S_3 nanopillars does not change in the case of the obliquely incident TE-polarized light (See Fig. S9a), the incident angle should not have a major effect on the output spectra. Likewise, since the this component of the electric field changes in the case of obliquely incident TM-polarized light (See Fig. S13b), we should see a greater impact of varying θ on the resulting spectra.

VII. INFLUENCE OF DIFFERENT DESIGN PARAMETERS

Analysis must also be done to determine the effects that the physical dimensions of the nanopillars have on the reflection spectrum. Fig. S14a,b,c show the reflectivity spectrum of a Sb_2S_3 array with nanopillars Fig 1b of varying heights (h), periods (p), and diameters (d). A control case is picked with $h = 120$ nm, $p = 390$ nm, and $d = 0.6p$. Fig. S14a shows the effect of varying h from 100 nm to 400 nm in the control case. This figure shows that few values of h give sharp reflections. Increasing the height past 100 nm causes a redshift in the reflection and a severe broadening of the reflection spectrum, until it decreases around $h = 300$ nm and ultimately disappears around $h = 400$ nm. Also, around $h = 200$ nm, another reflection appears in the spectrum. Increasing h beyond this point causes a redshift without the same

severe broadening.

Fig. S14b shows the effect of varying p from 200 nm to 500 nm in the control case. Fig. S14b shows that increasing p causes a redshift in the reflection spectrum throughout this test case. Also, the reflected spectrum narrows by increasing p from around $p = 200$ nm to around $p = 400$ nm. Fig. 14c shows the effect of varying d from $d = 150$ nm to $d = 350$ nm. Figure S8c shows that increasing d from 150 nm causes a redshift in the resulting spectrum. This peak decreases for $d > 250$ nm. However, another peak starts to appear around $d > 250$ nm and remains at larger values if d in this range. This new peak does not experience a red shift with an increase in d , but another, narrower, peak starts to appear with the increase in d . The change from amorphous to crystalline Sb_2S_3 has a nearly uniform effect in all these cases. The phase change to crystalline severely decreases the reflectivity of the metasurface and causes a redshift at the same time.

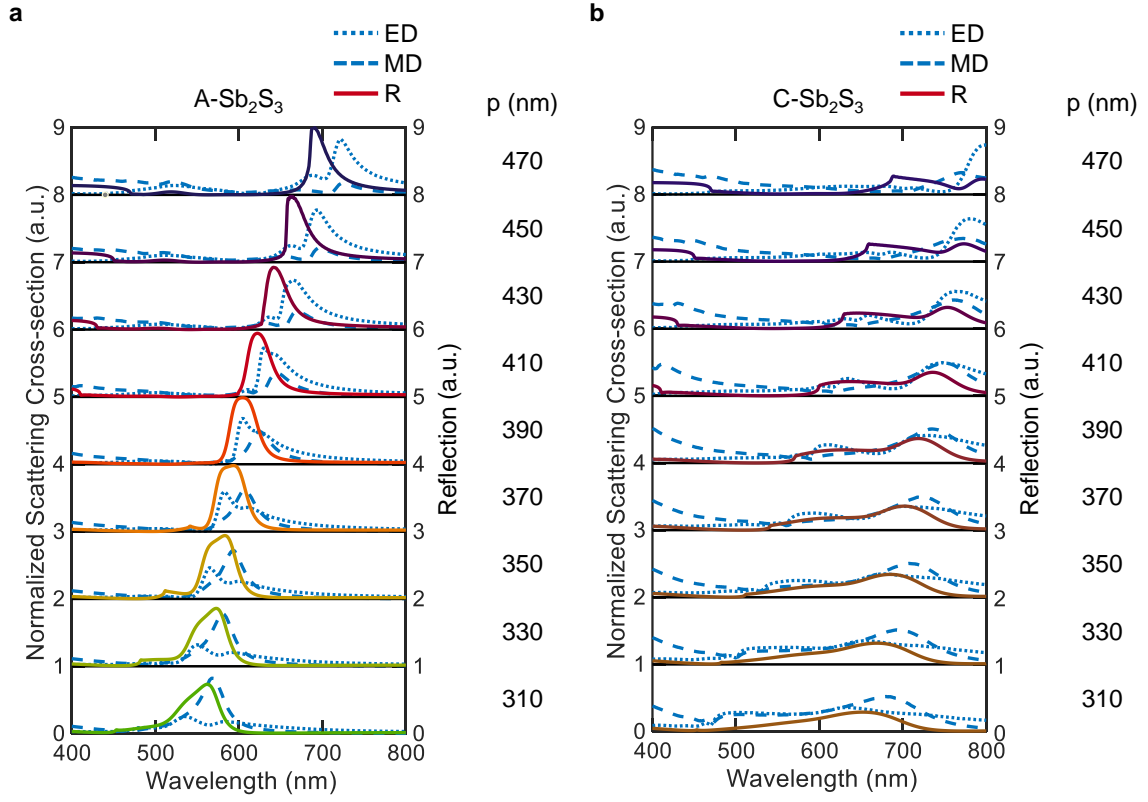


Figure S1. **Multipolar decomposition analysis.** **a,b**, Multipolar decomposition of scattering cross-section in terms of electric dipole (ED, the dotted lines) and magnetic dipole (MD, the dashed lines) for the case of an periodic array of **(a)** amorphous and **(b)** crystalline Sb_2S_3 nanopillars with $h = 120$ nm, $d = 0.6p$ in a lattice with varying periodicity of p on top of a SiO_2 substrate. The reflectance (R) response for each case is plotted in solid lines.

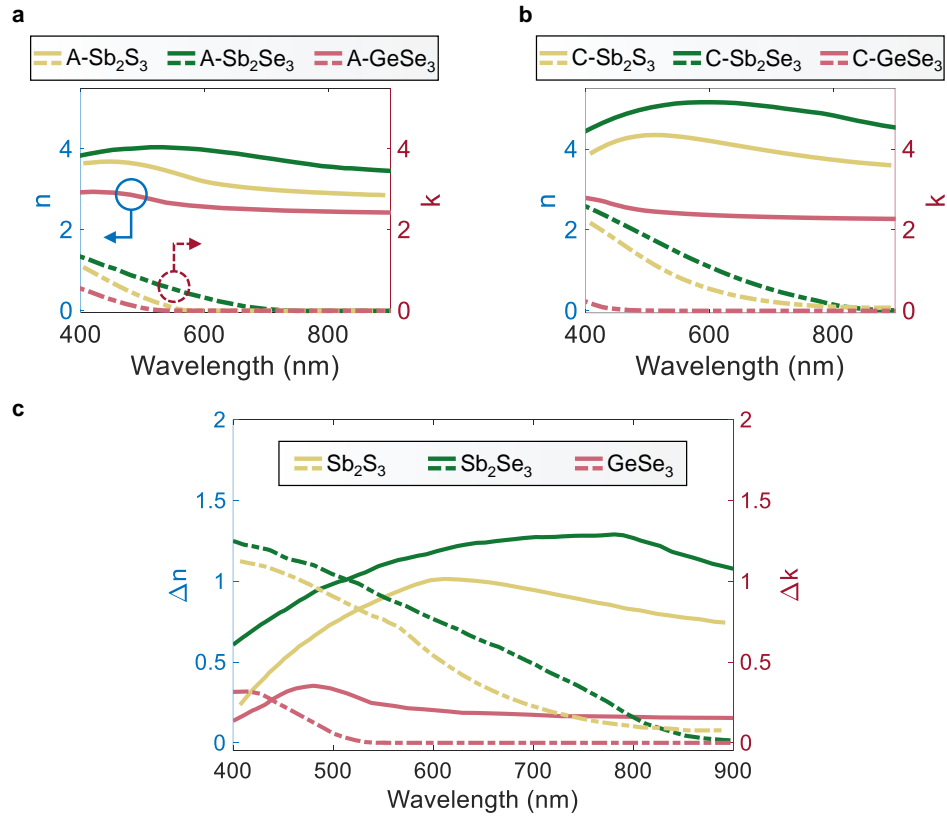


Figure S2. **Optical characteristics of low-loss phase-change materials.** **a,b**, Real (solid lines) and imaginary (dashed lines) parts of the refractive index of Sb_2S_3 , Sb_2Se_3 , and GeSe_3 for (a) amorphous (A) and (b) crystalline (C) phases. **c**, The absolute value of the change in the refractive index (solid lines, $\Delta n = |n_{\text{C-PCM}} - n_{\text{A-PCM}}|$) and the extinction coefficient (dashed lines, $\Delta k = |k_{\text{C-PCM}} - k_{\text{A-PCM}}|$) versus the wavelength upon the transition between amorphous and crystalline phase-states for Sb_2S_3 , Sb_2Se_3 and GeSe_3 .

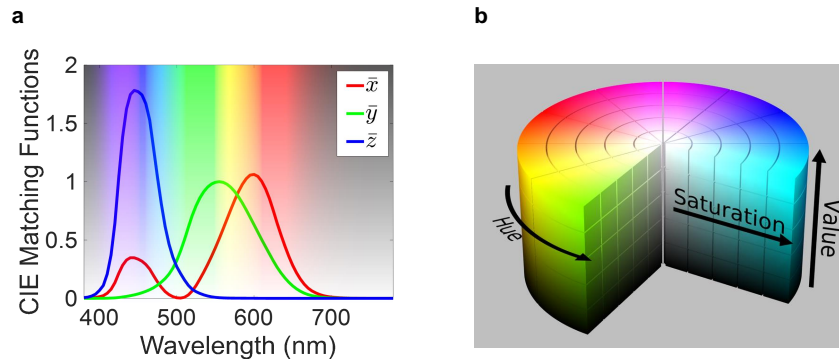


Figure S3. **Color generation and characteristics.** **a**, CIE 1931 standard color-matching functions. **b**, HSV color solid cylinder saturation gray [11].

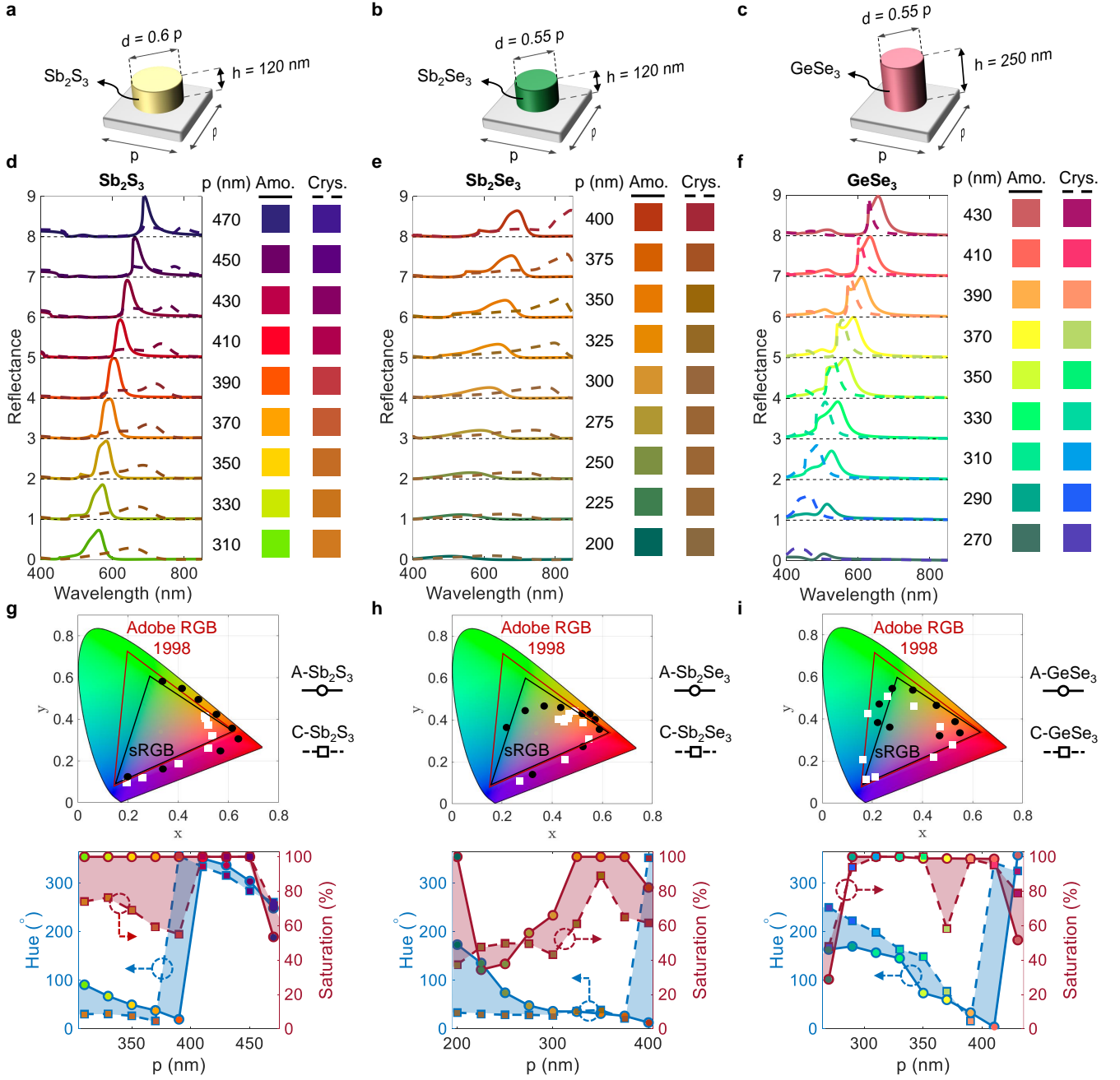


Figure S4. **Color switching enabled by phase-transition of the PCM nanopillars.** **a-c**, Schematic and geometrical parameters of a unit cell of a polarization-insensitive PCM metasurface made of **(a)** Sb_2S_3 , **(b)** Sb_2Se_3 and **(c)** GeSe_3 circular nanopillars with a fixed height h . The periodicity of the unit cell in both x and y directions is p , and the diameter of the nanopillars is $d = \alpha p$ with α being a constant. **d-f**, Simulated reflectance spectra for the amorphous (solid lines) and crystalline (dashed lines) phases and their corresponding colors for different periodicities (p). The PCM is **(d)**, **(e)**, and **(f)** is Sb_2S_3 , Sb_2Se_3 , and GeSe_3 , respectively. The curves for different p s are displaced vertically for better visibility and comparison. The sharp resonances observed in **(d-f)** are attributed to the interference between ED and MD modes inside the PCM nanopillars. Upon the PCM phase transition, a red-shift of $|\Delta\lambda_{\text{Sb}_2\text{S}_3}| > 180$ nm and $|\Delta\lambda_{\text{Sb}_2\text{Se}_3}| > 200$ nm is observed for the case of **(d)** Sb_2S_3 and **(e)** Sb_2Se_3 , respectively, while a blue-shift of $|\Delta\lambda_{\text{GeSe}_3}| < 70$ nm is observed for the case of **(f)** GeSe_3 . **g-i**, Corresponding CIE 1931 chromaticity coordinates of the reflectance spectra, and the hue and saturation values of the colors shown in **(d-f)** for amorphous (black circles in the top panel and circle-solid line in bottom panel) and crystalline (white squares in the top panel and square-dashed line in the bottom panel) phases of the corresponding PCMs in **(d-f)**.

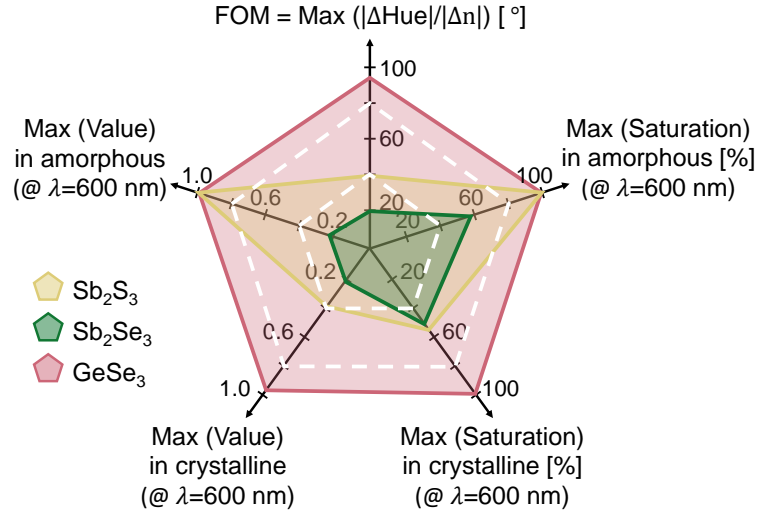


Figure S5. **Comparison of low-loss PCMs for color switching applications.** A spider chart that compares Sb_2S_3 , Sb_2Se_3 and GeSe_3 in terms of FOM (defined as the maximum (max) of $|\Delta\text{Hue}|/|\Delta n|$ in which $\Delta n = n_A(\lambda_A) - n_C(\lambda_C)$), maximum saturation and maximum value (i.e. the reflectance value at the resonance peak) in amorphous and crystalline phases at $\lambda_A = 600$ nm.

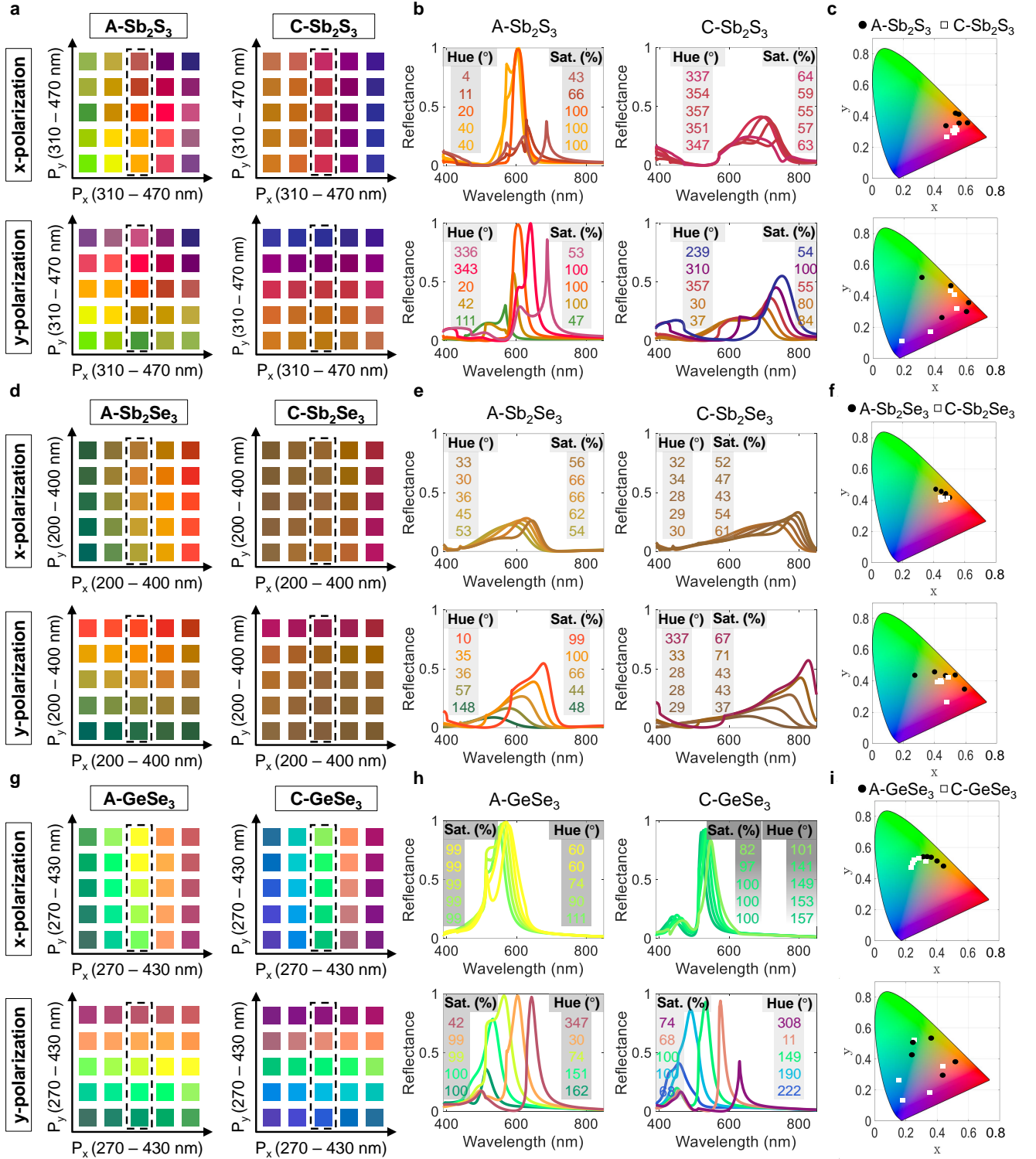


Figure S6. Multiple color generation enabled by phase-transition-based and polarization-based color switching mechanisms. **a,d,g**, Generated color palettes considering different periodicities in x - and y -directions (p_x and p_y , respectively) for (a) Sb₂S₃ ($\alpha = 0.6$ and $h = 120$ nm), (d) Sb₂Se₃ ($\alpha = 0.55$ and $h = 120$ nm), and (g) GeSe₃ ($\alpha = 0.55$ and $h = 250$ nm). p_x and p_y in (a), (d) and (g) vary with 40 nm, 50 nm, and 40 nm increments, respectively. **b,e,h**, Reflectance spectra of the colors indicated by the dashed rectangular boxes shown in the corresponding color palette in (a,d,g), respectively, with the values of hue and saturation (sat.) in the inset. **c,f,i**, Corresponding color gamuts for amorphous (black circles) and crystalline (white squares) phases of the corresponding PCM in (a,d,g), respectively. In each figure, the upper (lower) panel represents the results related to x -polarization (y -polarization).

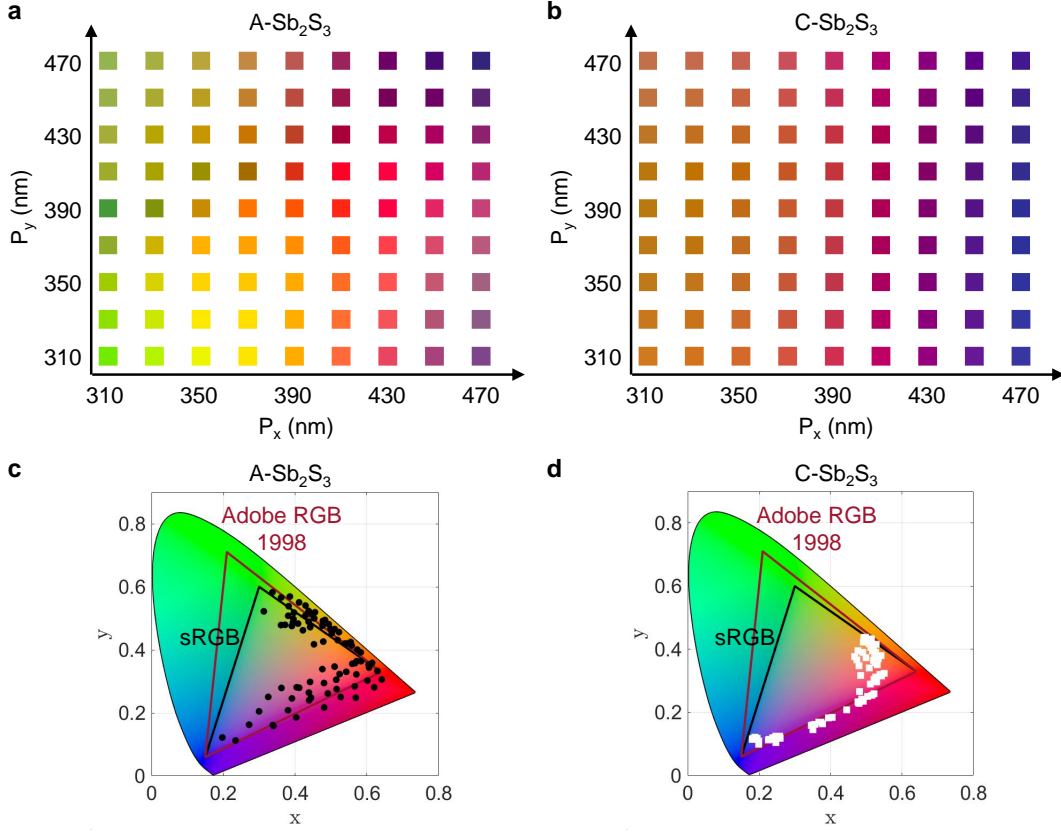


Figure S7. **Dynamic color generation by Sb_2S_3 meta-pixels.** **a,b**, The color palettes and **c, d**, corresponding CIE 1931 chromaticity diagrams generated by Sb_2S_3 metasurfaces in **(a, c)** amorphous and **(b, d)** crystalline phase-states under x-polarized normally incident white light. The lattice periodicities in x- and y-directions vary from $p_{x,y} = 310$ nm to $p_{x,y} = 470$ nm with a step of 20 nm while the diameter of the nanopillars changes as $d_{x,y} = 0.6 p_{x,y}$, and the height of the nanopillars is fixed at $h = 120$ nm.

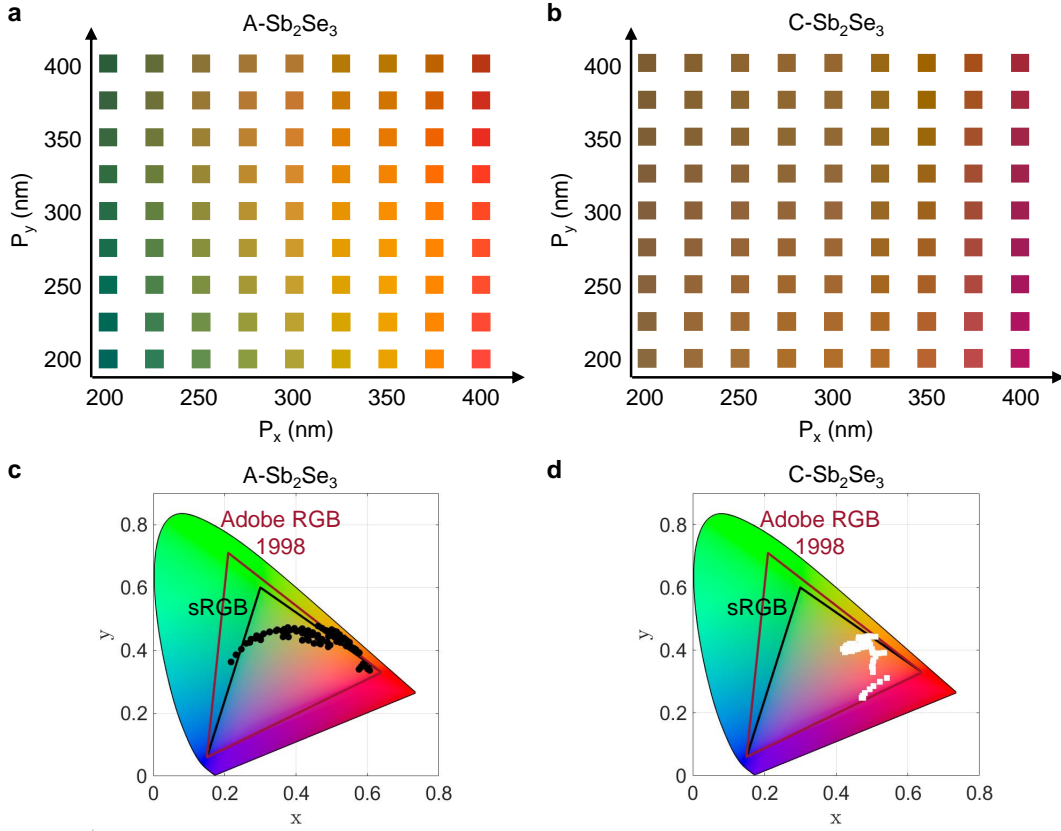


Figure S8. **Dynamic color generation by Sb_2Se_3 meta-pixels.** **a,b**, The color palettes and **c, d**, corresponding CIE 1931 chromaticity diagrams generated by Sb_2Se_3 metasurfaces in **(a, c)** amorphous and **(b, d)** crystalline phase-states under x-polarized normally incident white light. The lattice periodicities in x- and y-directions vary from $p_{x,y} = 200$ nm to $p_{x,y} = 400$ nm with a step of 25 nm while the diameter of the nanopillars changes as $d_{x,y} = 0.55 p_{x,y}$, and the height of the nanopillars is fixed at $h = 120$ nm.

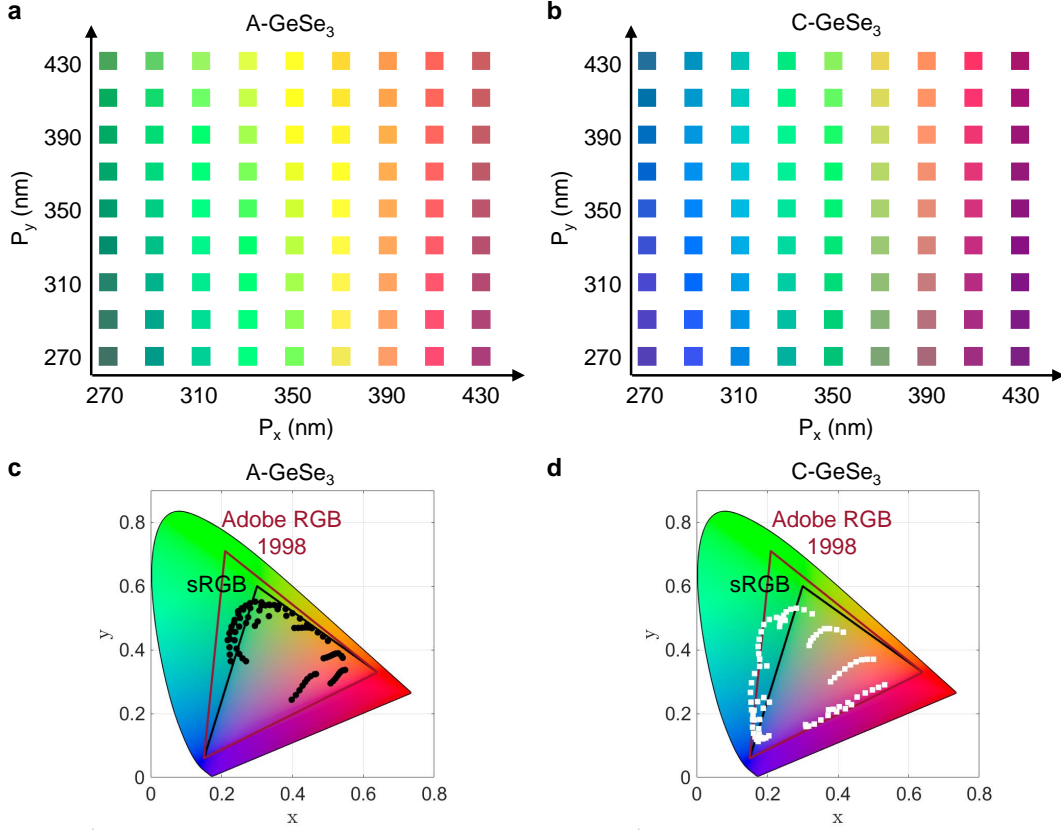


Figure S9. **Dynamic color generation by GeSe₃ meta-pixels.** **a,b**, The color palettes and **c, d**, corresponding CIE 1931 chromaticity diagrams generated by GeSe₃ metasurfaces in **(a, c)** amorphous and **(b, d)** crystalline phase-states under x-polarized normally incident white light. The lattice periodicities in x- and y-directions vary from $p_{x,y} = 270$ nm to $p_{x,y} = 430$ nm with a step of 20 nm while the diameter of the nanopillars changes as $d_{x,y} = 0.55 p_{x,y}$, and the height of the nanopillars is fixed at $h = 250$ nm.

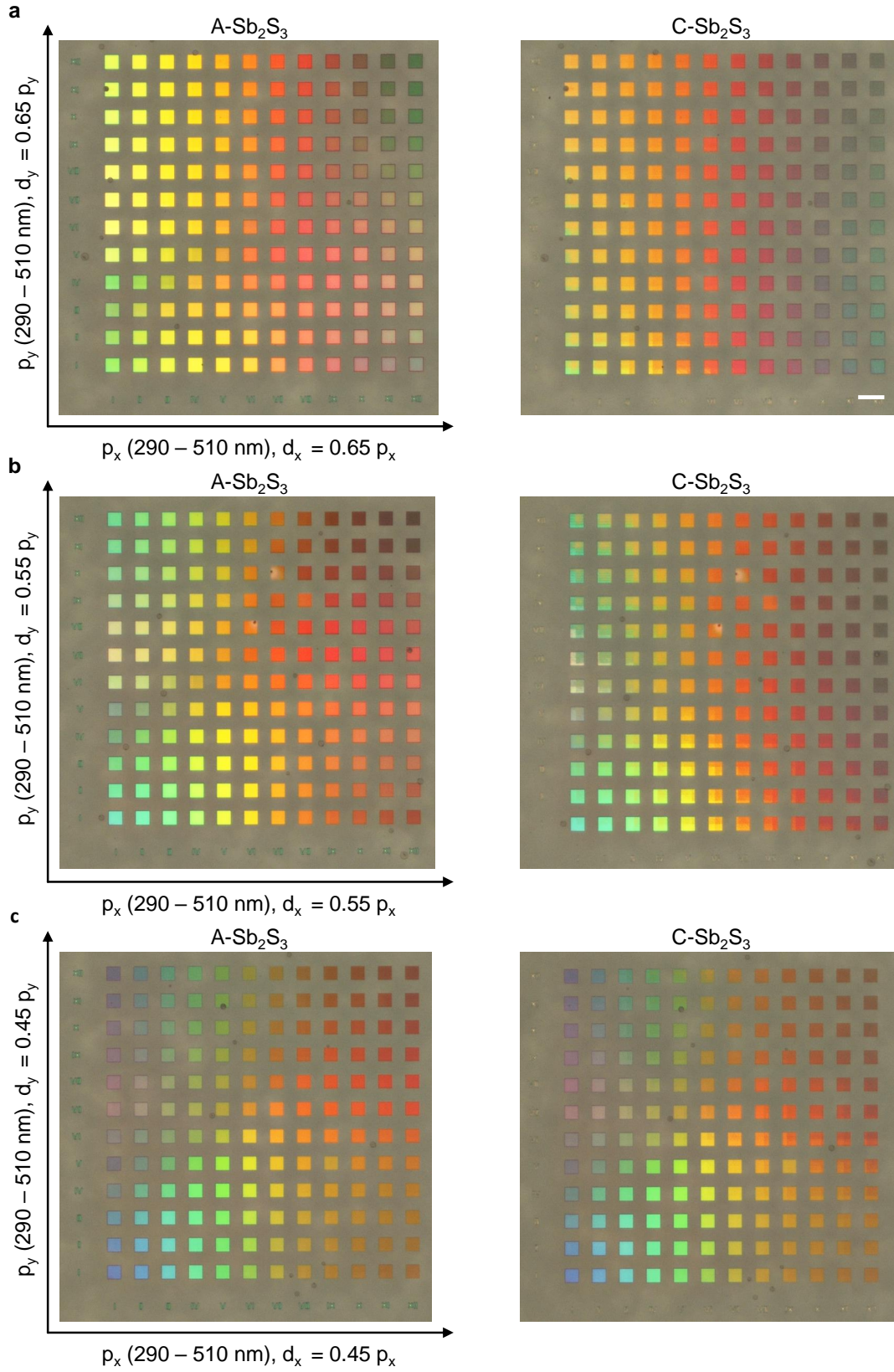


Figure S10. **Experimental color palettes of Sb₂S₃ meta-pixels a,b,c**, A-Sb₂S₃ (left) and C-Sb₂S₃ (right) meta-pixels considering different periodicities in x- and y- directions (p_x and p_y , respectively) varying with 20 nm increments while the diameter of the nanopillars changes as (a) $d_{x,y} = 0.65 p_{x,y}$, (b) $d_{x,y} = 0.55 p_{x,y}$, (c) $d_{x,y} = 0.45 p_{x,y}$, and the height of the nanopillars is fixed at $h = 120$ nm.

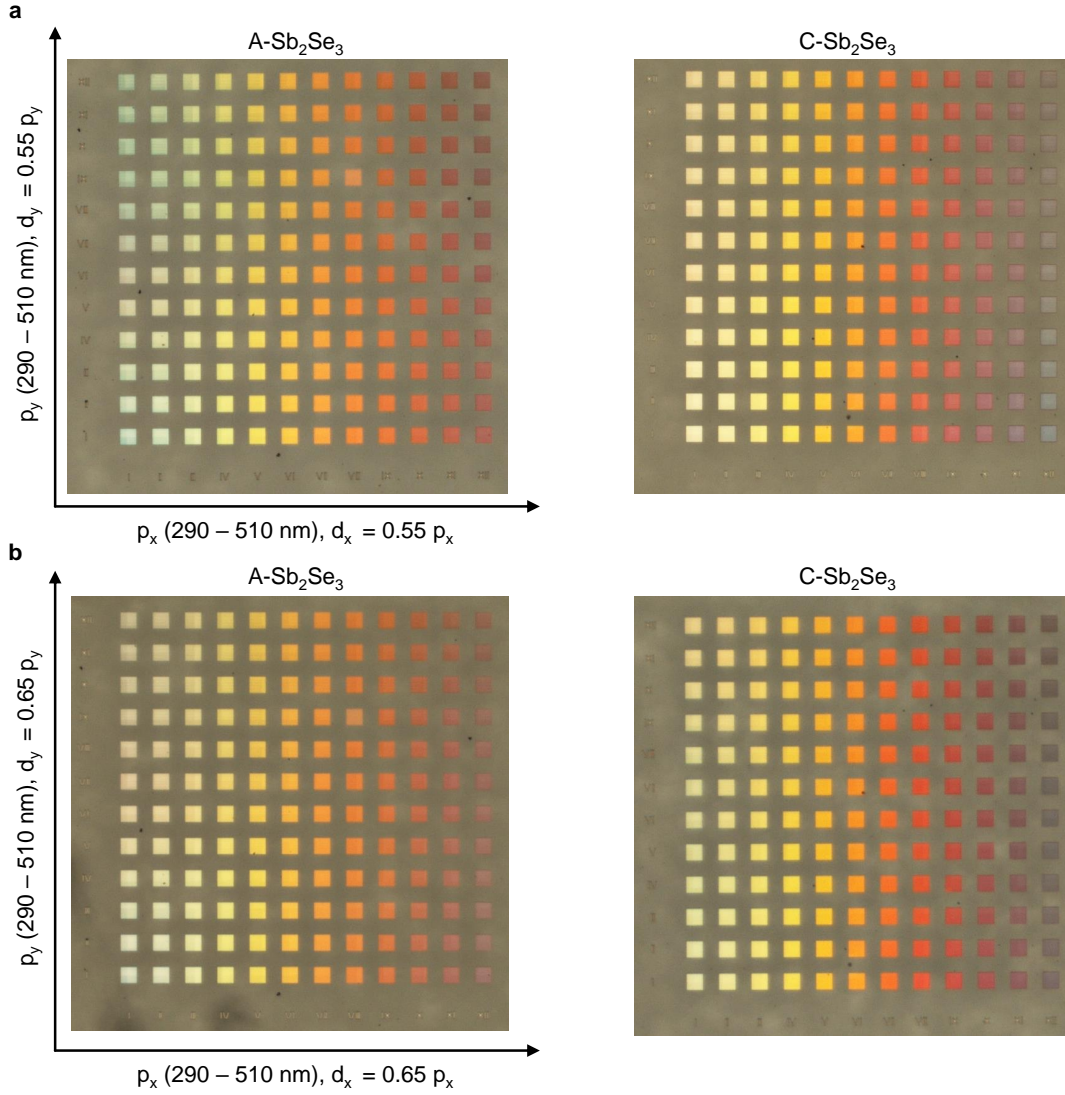


Figure S11. **Experimental color palettes of Sb_2Se_3 meta-pixels a,b**, A- Sb_2Se_3 (left) and C- Sb_2Se_3 (right) meta-pixels considering different periodicities in x- and y- directions (p_x and p_y , respectively) varying with 20 nm increments while the diameter of the nanopillars changes as (a) $d_{x,y} = 0.55 p_{x,y}$, (b) $d_{x,y} = 0.65 p_{x,y}$, and the height of the nanopillars is fixed at $h = 120$ nm. Sb_2Se_3 is sputtered in a magnetron sputtering system using 30 W radio frequency (RF) power at a deposition pressure of 4 mTorr and Ar flow of 30 sccm. The deposition rate for Sb_2Se_3 is ~ 1 nm/min. Before deposition, the chamber base pressure is maintained at $\sim 10^{-7}$ Torr. Additionally, the samples are capped with 15 nm of SiO_2 sputtered in situ, to prevent oxidation during later characterization. As an aside, several pre- and post-deposition treatments of the sputtering chamber are performed for selenide deposition. These include cleaning the chamber followed by annealing and O_2 plasma cleaning.

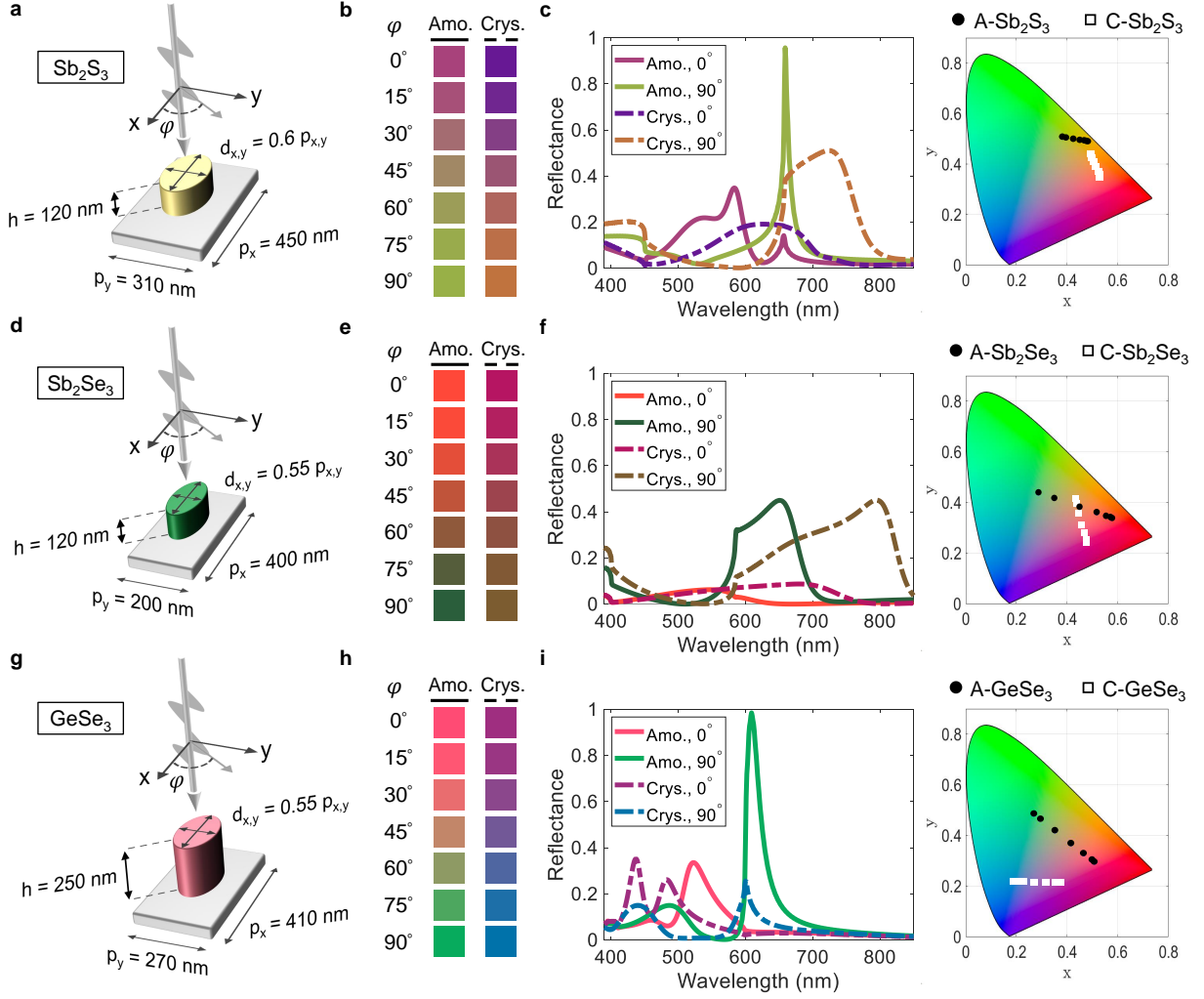


Figure S12. **Polarization-based continuous color-switching enabled by rotating the incident polarization angle.** The asymmetric unit cells of the polarization-sensitive metasurface with the optimized design parameters are shown in **a**, **d**, and **g**, respectively, with their corresponding variation of colors with polarization angle φ and their color gamts shown in **b**, **e**, and **h**, respectively. The simulated reflectance spectra from **c**, Sb_2S_3 , **f**, Sb_2Se_3 , and **i**, GeSe_3 metasurfaces for x-polarization ($\varphi = 90^\circ$) and y-polarization ($\varphi = 0^\circ$). The reflection-mode color response varies from reddish purple to the yellowish green for A- Sb_2S_3 , bluish purple to the reddish orange for C- Sb_2S_3 , red to dark green for A- Sb_2Se_3 , red purple to brown for C- Sb_2Se_3 , purple to green for A- GeSe_3 , and red purple to blue for C- GeSe_3 .

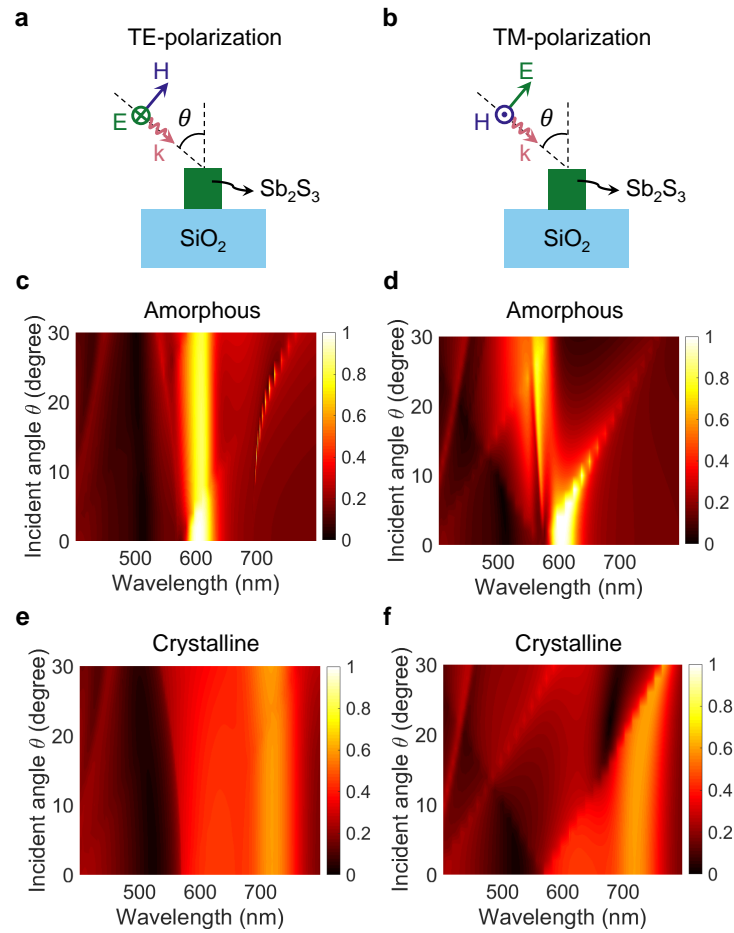


Figure S13. **Analysis of the sensitivity to the angle of incidence.** The structure used in the study of the angle sensitivity of a Sb_2S_3 metasurface for the case of obliquely incident plane waves of white light for **a**, TE and **b**, TM polarizations, respectively. **c,d,e,f**, The simulated reflection spectra of the metasurface, showing the incident angle (degrees) versus wavelength (nm) for: **(c)** amorphous phase and TE polarization, **(d)** amorphous phase and TM polarization, **(e)** crystalline phase and TE polarization, **(f)** crystalline phase and TM polarization.

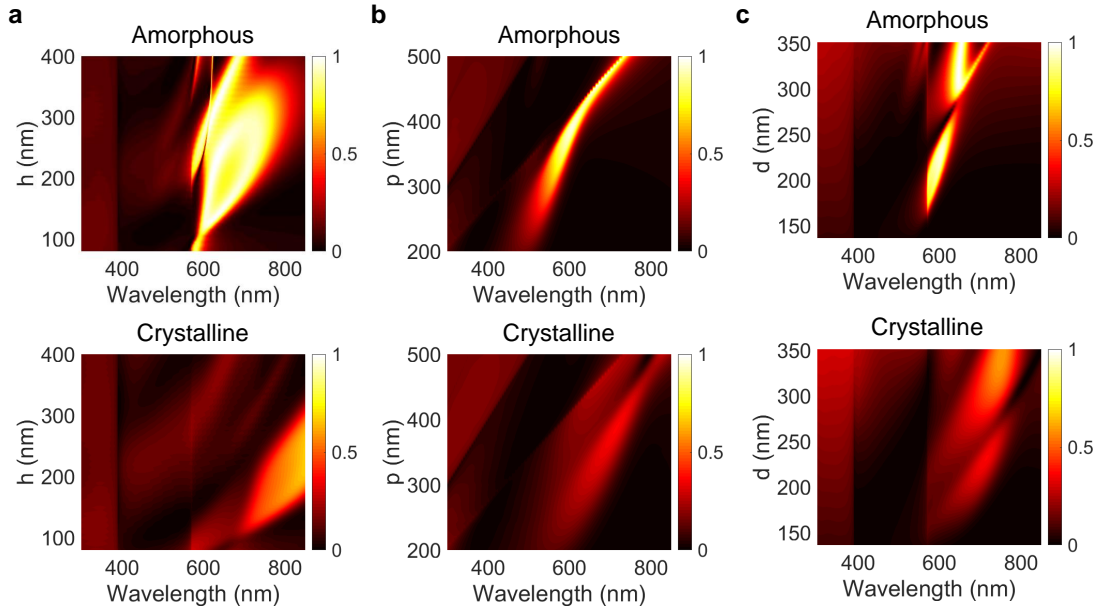














Figure S14. **Analysis of the effect of different design parameters.** Simulated reflection spectrum of the Sb_2S_3 metasurface in Figure 2a versus; **a**, The height of the constituents nanopillars, i.e., h , while other parameters are fixed at $p = 390$ nm and $d = 0.6p$ for (top) amorphous and (bottom) crystalline phases; **b**, period of the unit cell, i.e., p , with $d = 0.6p$ and $h = 120$ nm for (top) amorphous and (bottom) crystalline phases; **c**, diameter of the constituent nanopillars, i.e., d , with $p = 390$ nm and $h = 120$ nm for (top) amorphous and (bottom) crystalline phases.

Section #	p_x (nm)	p_y (nm)	Color in Amo./x-pol.	Color in Crys./x-pol.
1	470	370		
2	470	410		
3	470	430		
4	470	450		
5	350	310		
6	470	470		

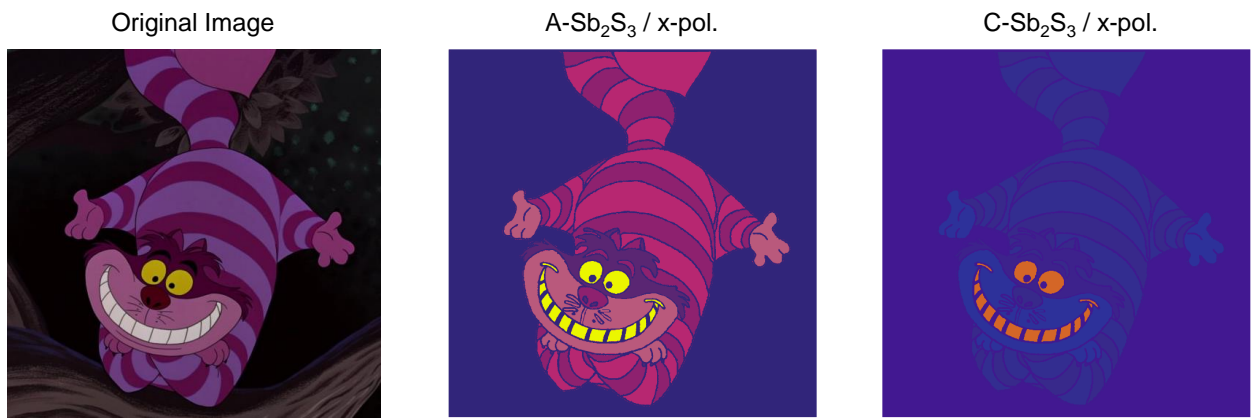
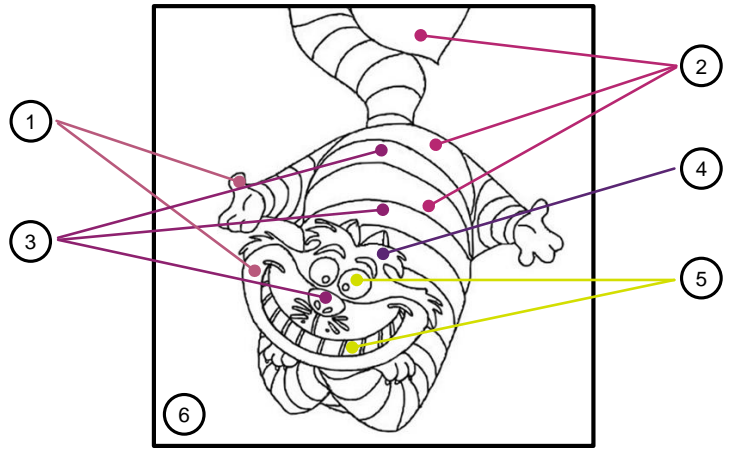


Figure S15. **Design strategy for generating the dynamic image of Cheshire The Cat.** The geometrical parameters of the Sb_2S_3 metasurfaces used for producing each pixel of the image of Cheshire The Cat shown in Fig. 3a in the main text ($d_{x,y} = 0.65 p_{x,y}$ and $h = 120$ nm in Fig. 1b).

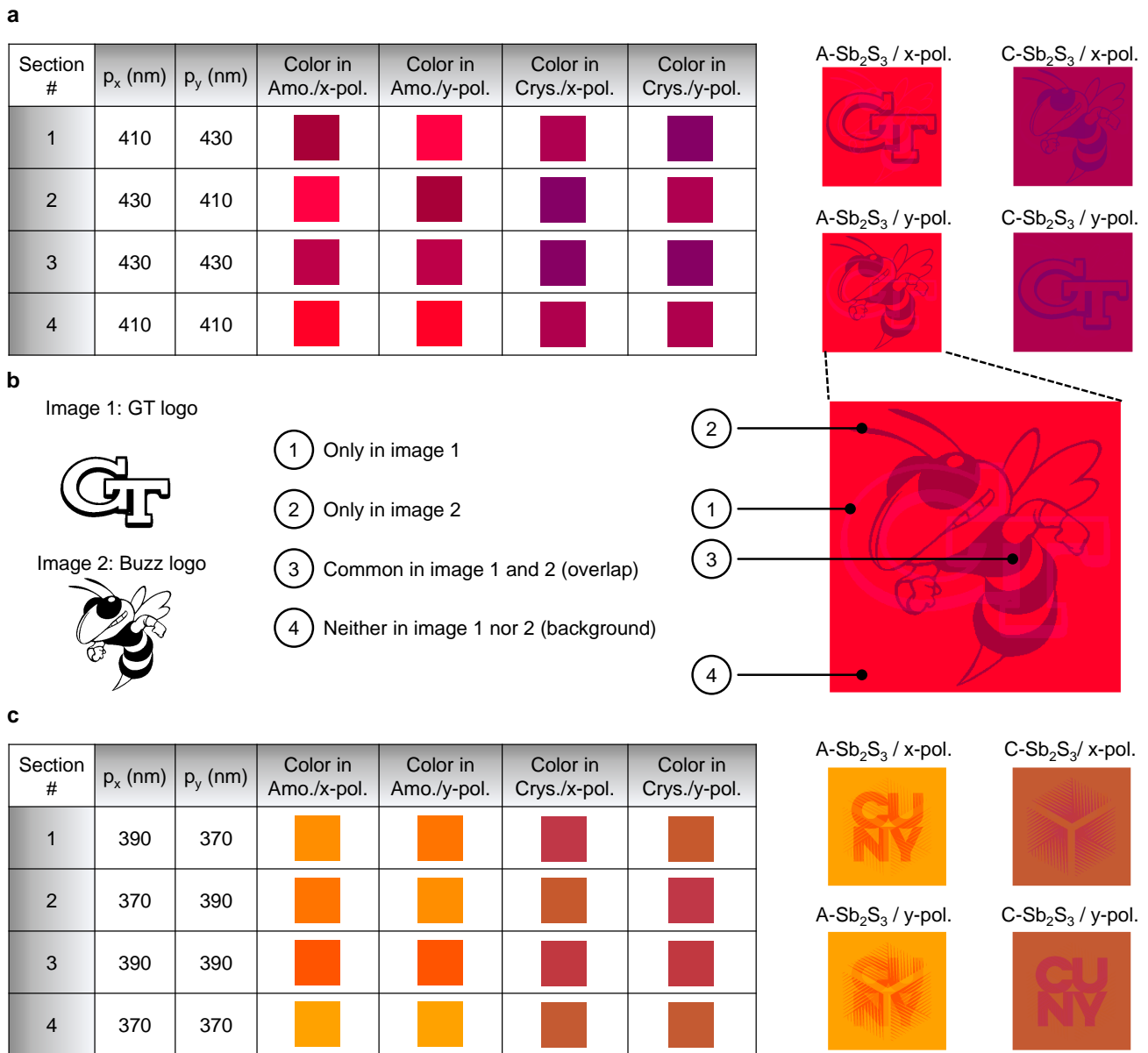


Figure S16. **Design strategy for encryption of four different images into the phase and polarization of Sb₂S₃ meta-pixels.** **a,c**, Phase-transition-based switching between two different images. The colors are generated by four different metasurfaces consisting of Sb₂S₃ nanopillars (Fig. 1b) with periodicities reported in the table, diameters $d_{x,y} = 0.65 p_{x,y}$, and a fixed height $h = 120$ nm. **b**, The definition of different zones in each image.

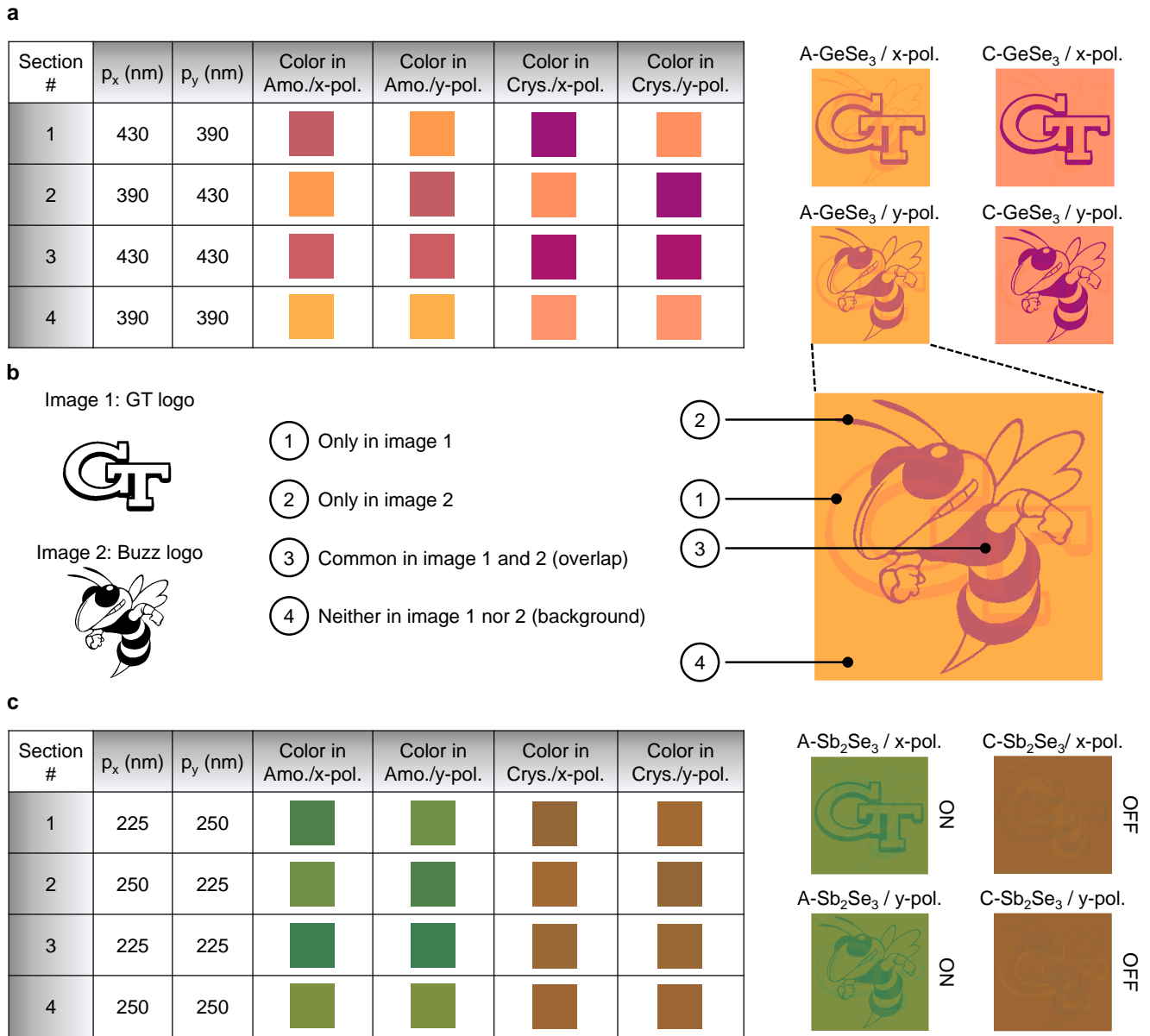


Figure S17. **Design strategy for encryption of four different images into the phase and polarization of Sb₂Se₃ and GeSe₃ meta-pixels.** **a**, Polarization-based switching between two different images. The colors are generated by four different metasurfaces consisting of GeSe₃ nanopillars (Fig. S3b) with periodicities reported in the table, diameters of $d_{x,y} = 0.55 p_{x,y}$, and a fixed height $h = 250$ nm. **b**, The definition of different zones in each image. **c**, Phase-transition-based switching between the ON-state (amorphous) and the OFF-state (crystalline). The colors are generated by four different metasurfaces consisting of Sb₂Se₃ nanopillars with periodicities reported in the table, diameters $d_{x,y} = 0.55 p_{x,y}$, and a fixed height $h = 120$ nm.

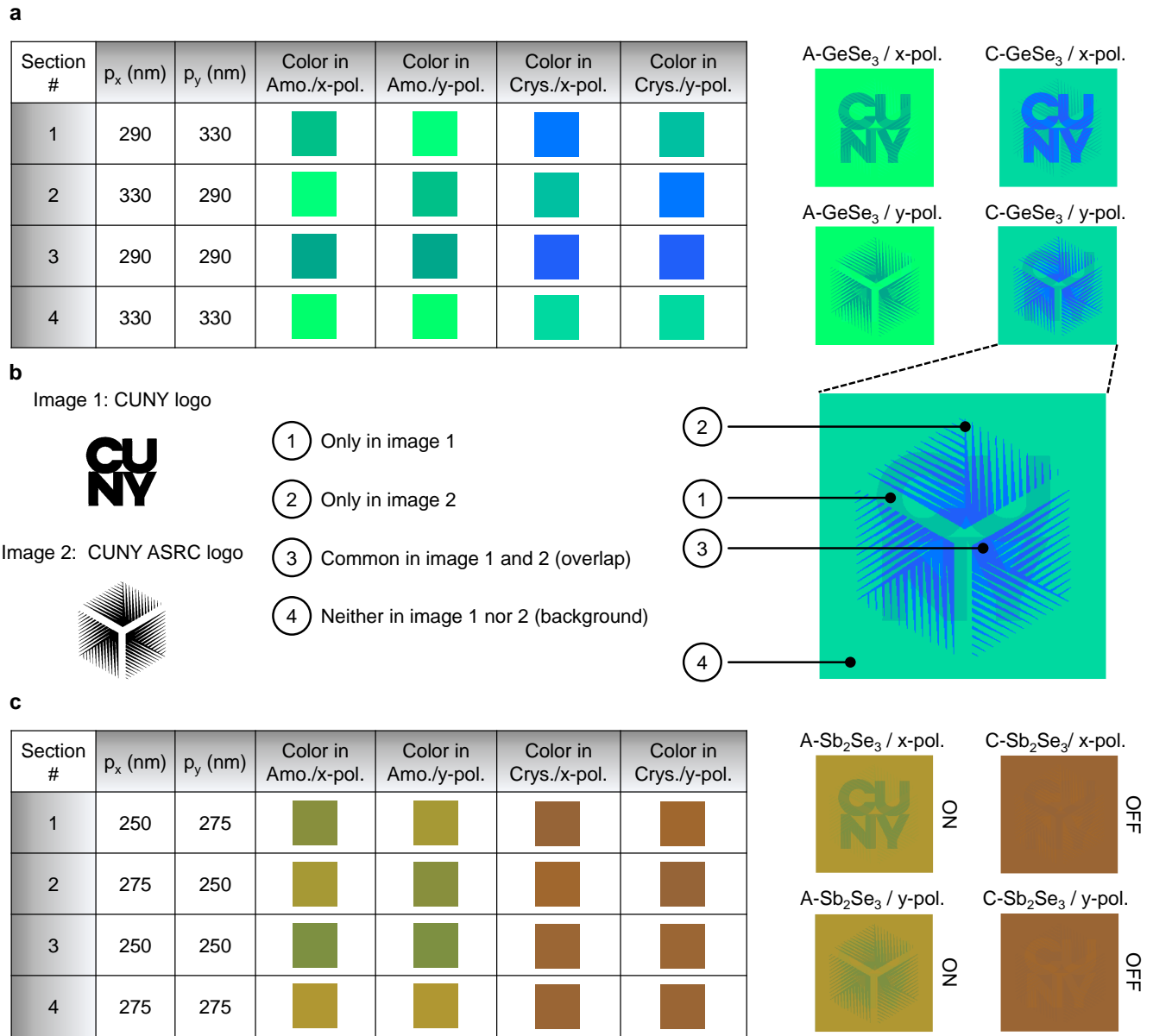


Figure S18. **Design strategy for encryption of four different images into the phase and polarization of Sb₂Se₃ and GeSe₃ meta-pixels.** **a**, Polarization-based switching between two different images. The colors are generated by four different metasurfaces consisting of GeSe₃ nanopillars (Fig. S3b) with periodicities reported in the table, diameters $d_{x,y} = 0.55 p_{x,y}$, and a fixed height $h = 250$ nm. **b**, The definition of different zones in each image. **c**, Phase-transition-based switching between the ON-state (amorphous) and the OFF-state (crystalline). The colors are generated by four different metasurfaces consisting of Sb₂Se₃ nanopillars with periodicities reported in the table, diameters $d_{x,y} = 0.55 p_{x,y}$, and a fixed height $h = 120$ nm.

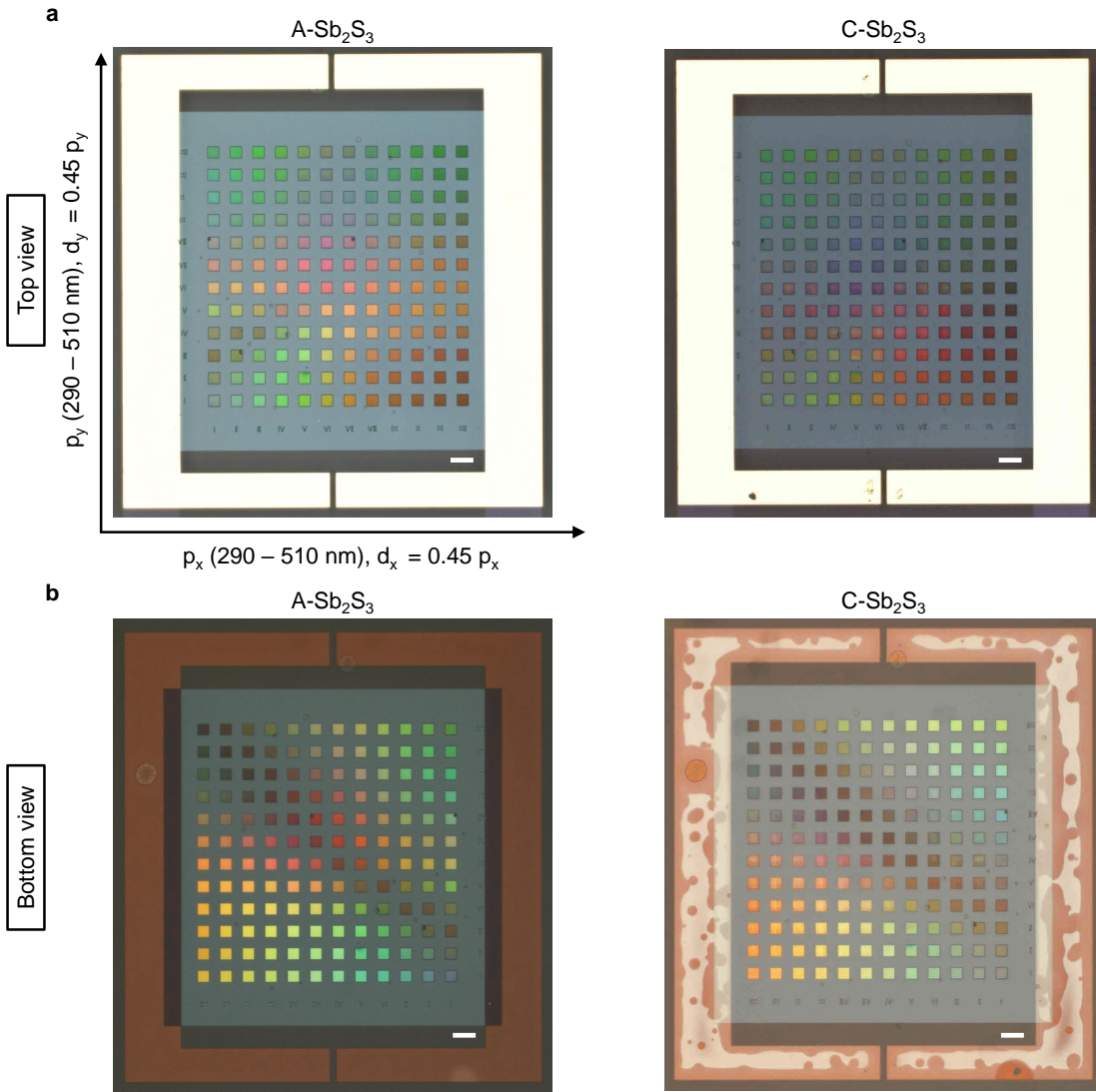


Figure S19. **Electrical conversion of color palettes of Sb₂S₃ meta-pixels using ITO heater.** a,b, A-Sb₂S₃ (left) and C-Sb₂S₃ (right) meta-pixels observed from (a) top and (b) bottom of the sample considering different periodicities in x- and y- directions (p_x and p_y , respectively) varying with 20 nm increments while the diameter of the Sb₂S₃ nanopillars changes as $d_{x,y} = 0.45 p_{x,y}$, and the height of the nanopillars is fixed at $h = 120$ nm. The scale bars are 100 μ m.

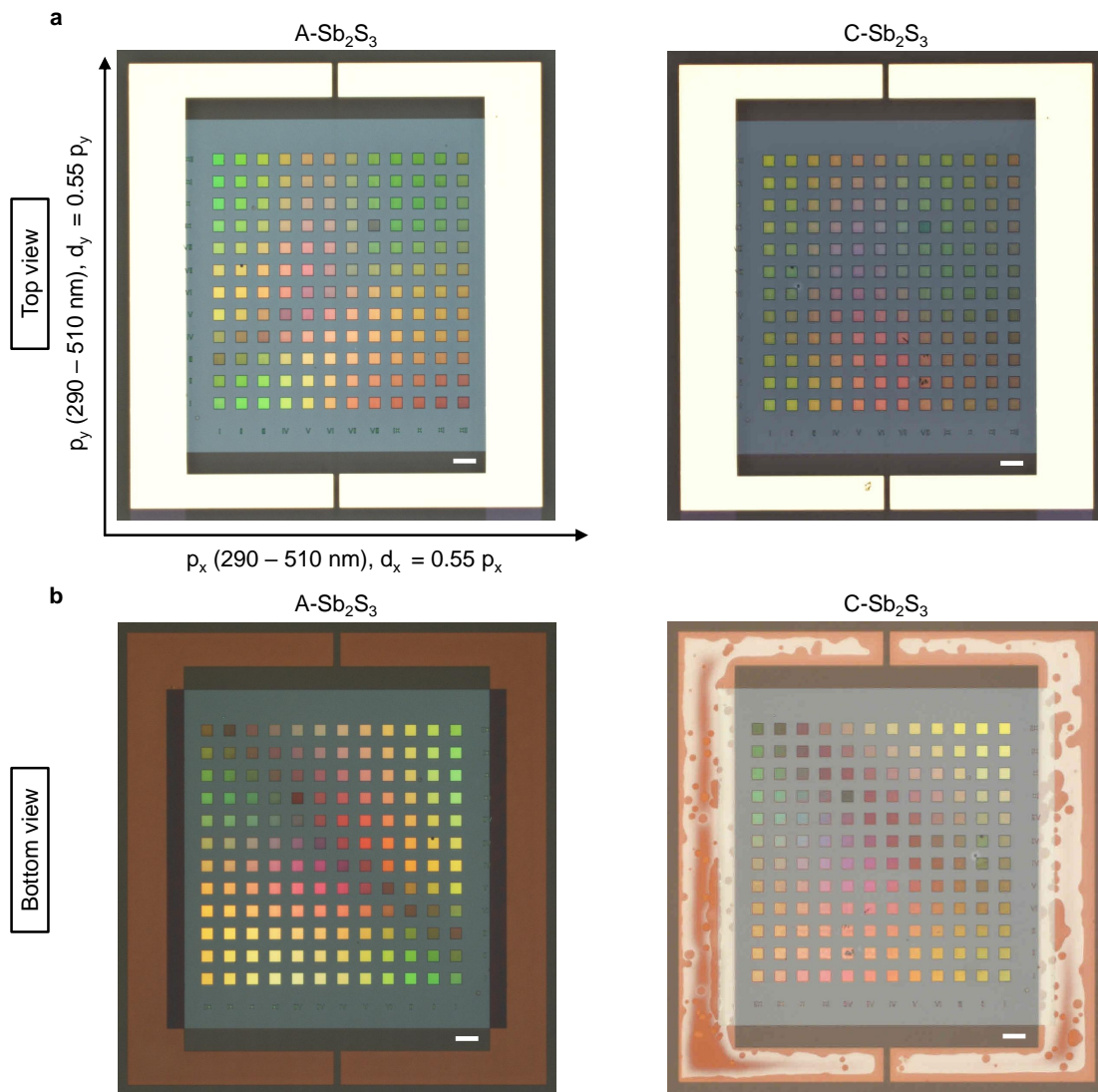


Figure S20. **Electrical conversion of color palettes of Sb₂S₃ meta-pixels using ITO heater.** a,b, A-Sb₂S₃ (left) and C-Sb₂S₃ (right) meta-pixels observed from (a) top and (b) bottom of the sample considering different periodicities in x- and y- directions (p_x and p_y , respectively) varying with 20 nm increments while the diameter of the Sb₂S₃ nanopillars changes as $d_{x,y} = 0.55 p_{x,y}$, and the height of the nanopillars is fixed at $h = 120$ nm. The scale bars are 100 μ m.

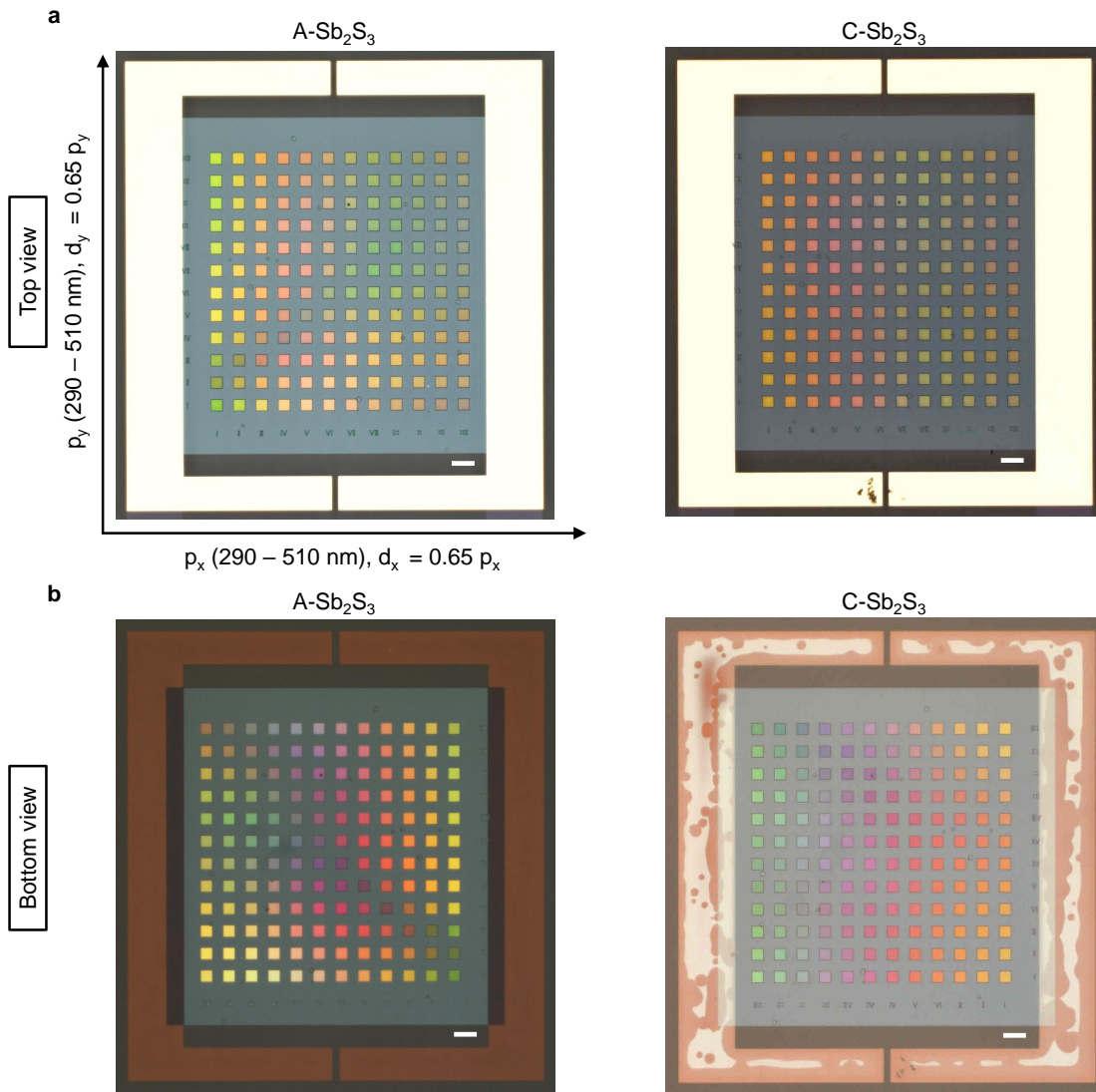


Figure S21. **Electrical conversion of color palettes of Sb₂S₃ meta-pixels using ITO heater.** a,b, A-Sb₂S₃ (left) and C-Sb₂S₃ (right) meta-pixels observed from (a) top and (b) bottom of the sample considering different periodicities in x- and y- directions (p_x and p_y , respectively) varying with 20 nm increments while the diameter of the Sb₂S₃ nanopillars changes as $d_{x,y} = 0.65 p_{x,y}$, and the height of the nanopillars is fixed at $h = 120$ nm. The scale bars are 100 μ m.

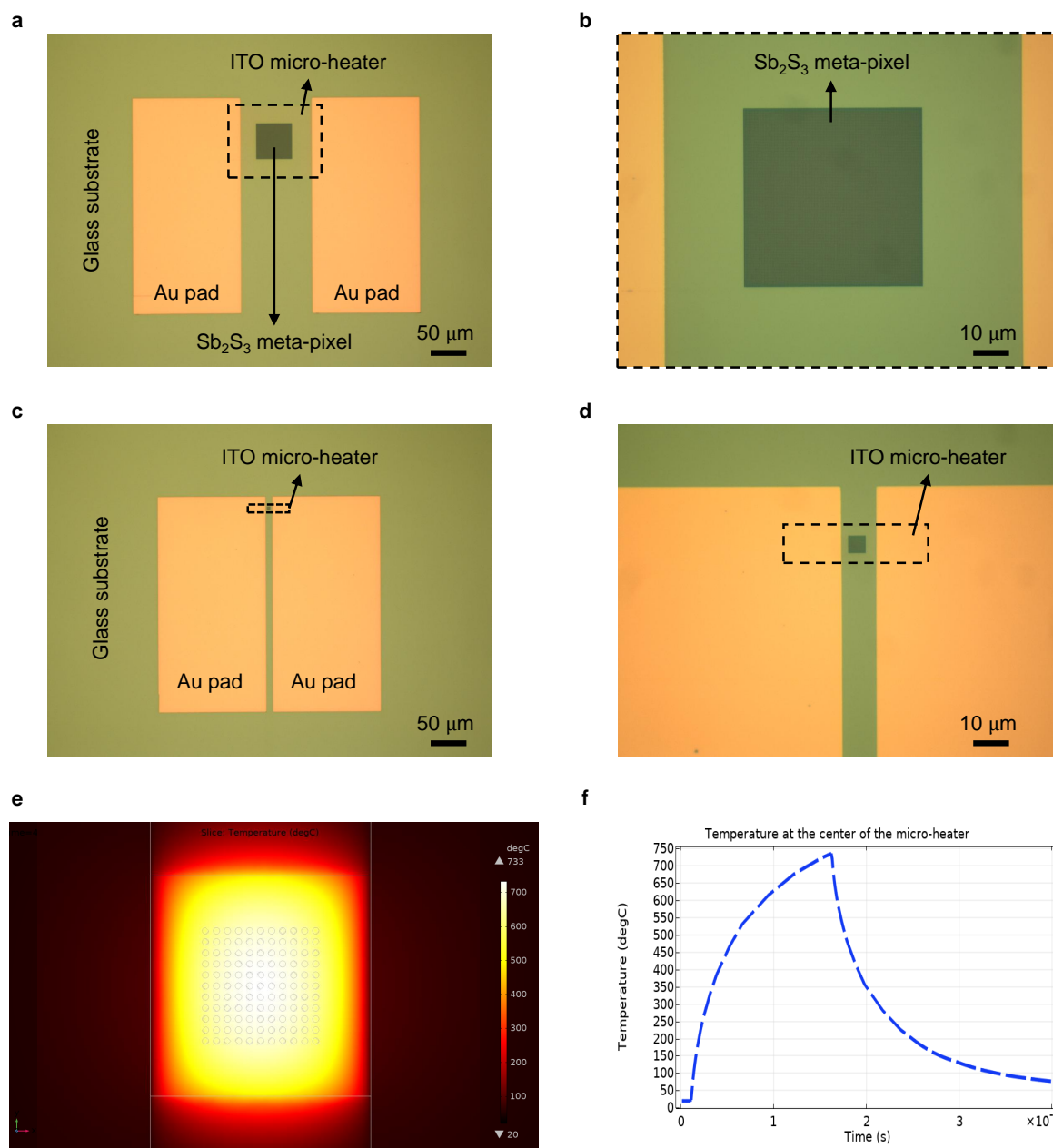
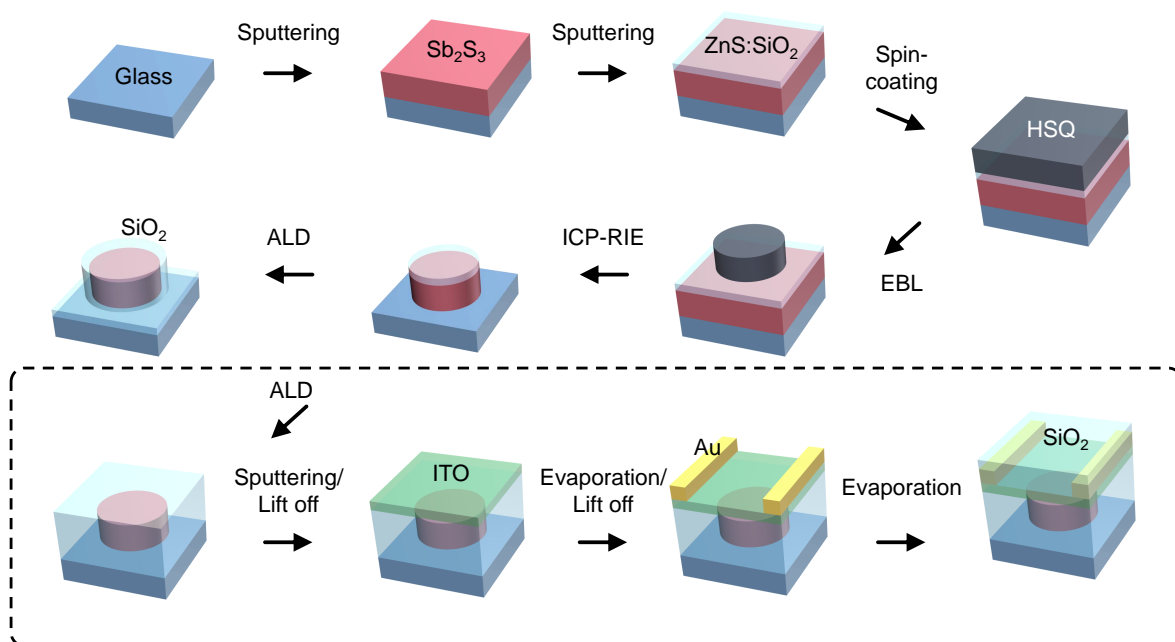
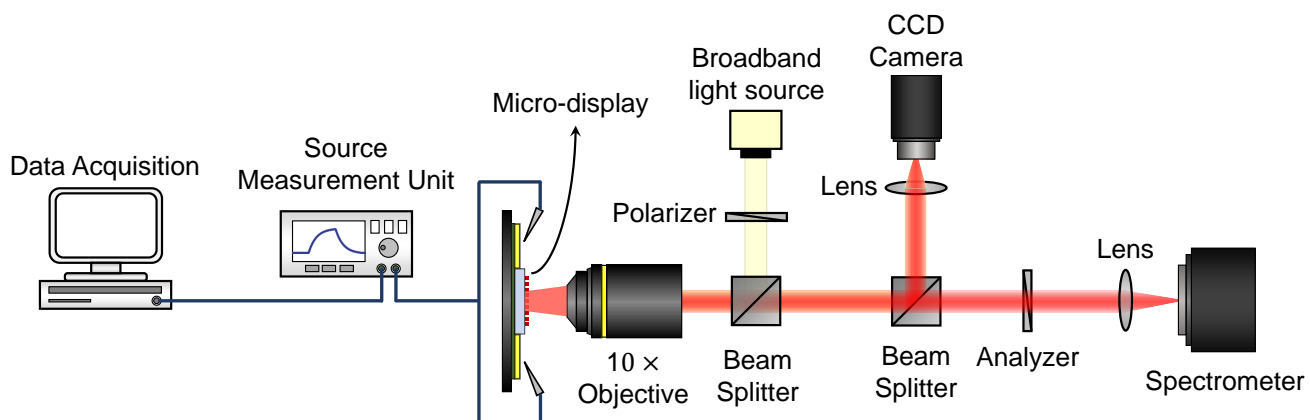


Figure S22. **Electrical conversion of a Sb_2S_3 meta-pixel using ITO micro-heater.** a-d, Microscope images of (a,b) $100 \times 100 \mu\text{m}^2$, and (c,d) $10 \times 10 \mu\text{m}^2$ micro-heaters with $50 \times 50 \mu\text{m}^2$ and $5 \times 5 \mu\text{m}^2$ meta-pixels at the center, respectively. e, Simulated temperature distribution in the cross-section of the meta-pixel in (d) at the end of a 7 V pulse with $15 \mu\text{s}$ duration. d, Real-time temperature profile at the center of the meta-pixel upon applying the re-amorphization pulse to the microheater.

Figure S23. **Fabrication process.**Figure S24. **Optical characterization setup.**

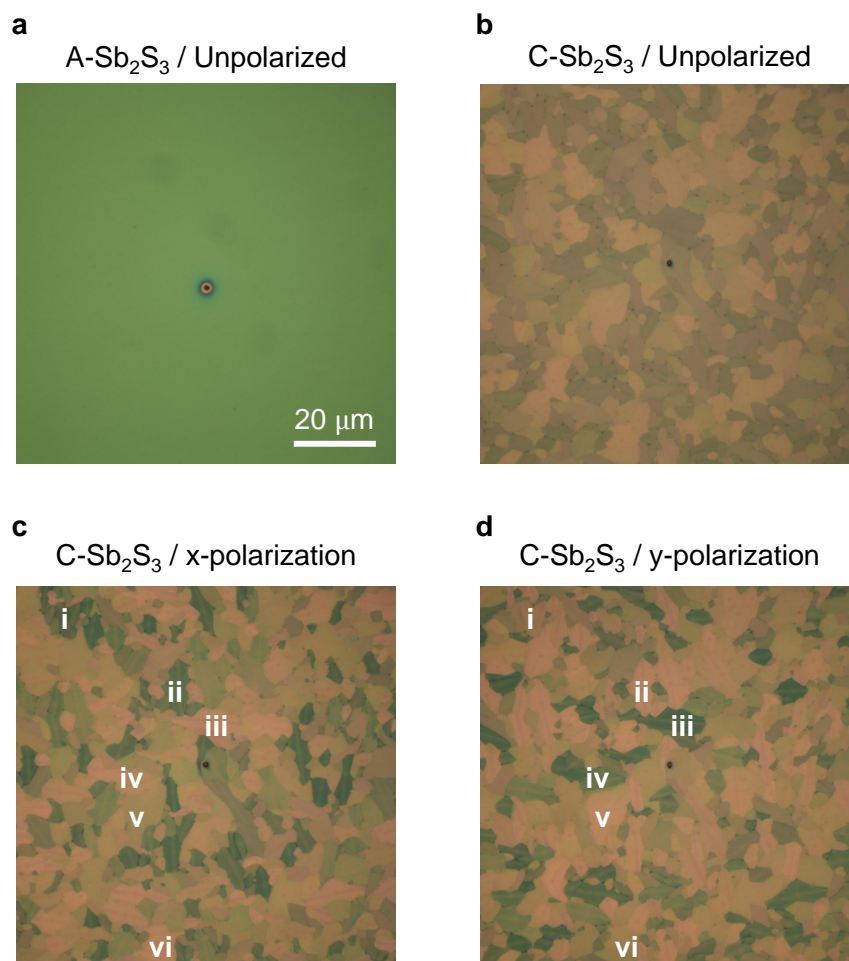


Figure S25. **Characterization of the anisotropic C-Sb₂S₃ crystals.** a-d, Optical images a film of (a) A-Sb₂S₃ and (b-d) C-Sb₂S₃ under microscope with (b) unpolarized, (c) x- and (d) y-polarized incident white light. The crystalized regions at (i) and (ii) switches from greenish colors to brownish ones going from x- to y-polarization, while colors in regions (iii) and (iv) changes from brownish to greenish, and colors in areas (v) and (vi) remains the almost unchanged. The dark particle at the center of the images is used as the marker for positioning.

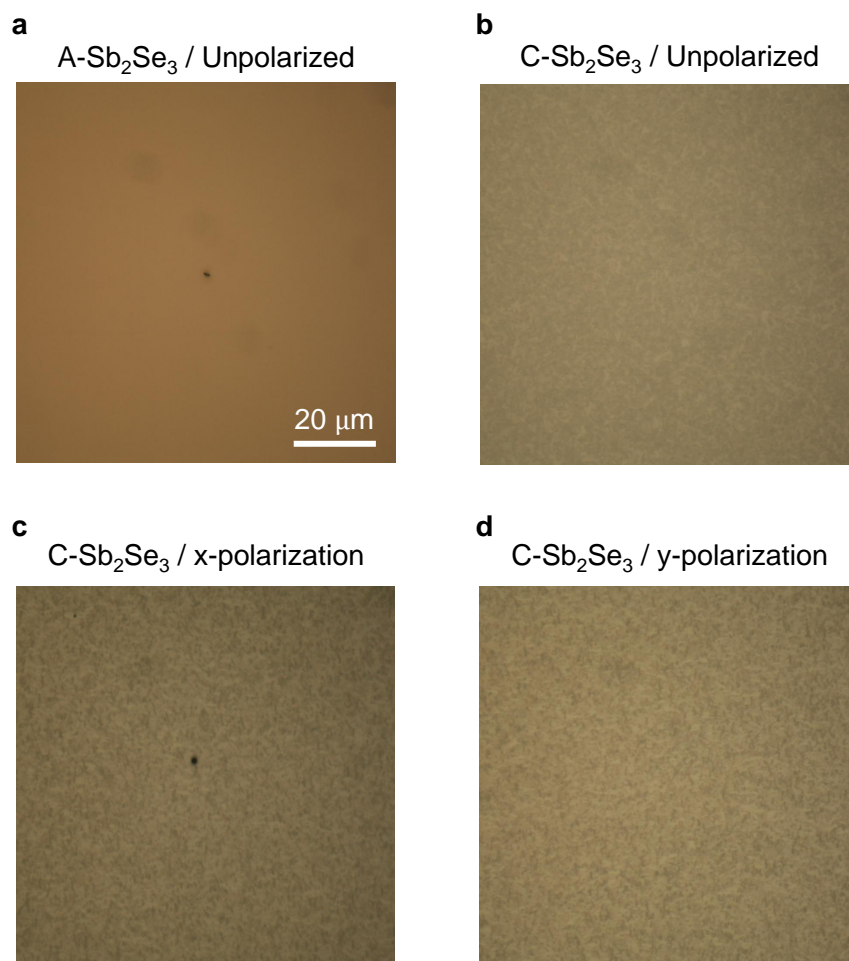


Figure S26. **Characterization of the anisotropic C-Sb₂Se₃ crystals.** **a-d**, Optical images a film of **(a)** A-Sb₂Se₃ and **(b-d)** C-Sb₂Se₃ under microscope with **(b)** unpolarized, **(c)** x- and **(d)** y-polarized incident white light. The dark particle at the center of the images is used as the marker for positioning.